Fluidization of Nanosized Particles by a Microjet and Vibration Assisted (MVA) Method

by

Keju An

A Dissertation Presented in Partial Fulfillment
of the Requirements for the Degree
Doctor of Philosophy

Approved November 2019 by the
Graduate Supervisory Committee:

Jean Andino, Co-Chair
Patrick Phelan, Co-Chair
Ronald Adrian
Heather Emady
Mohamed Kasbaoui

ARIZONA STATE UNIVERSITY

December 2019

ABSTRACT

The applications utilizing nanoparticles have grown in both industrial and academic areas because of the very large surface area to volume ratios of these particles. One of the best ways to process and control these nanoparticles is fluidization. In this work, a new microjet and vibration assisted (MVA) fluidized bed system was developed in order to fluidize nanoparticles. The system was tested and the parameters optimized using two commercially available TiO_2 nanoparticles: P25 and P90. The fluidization quality was assessed by determining the non-dimensional bed height as well as the non-dimensional pressure drop. The non-dimensional bed height for the nanosized TiO_2 in the MVA system optimized at about 5 and 7 for P25 and P90 TiO_2, respectively, at a resonance frequency of 50 Hz. The non-dimensional pressure drop was also determined and showed that the MVA system exhibited a lower minimum fluidization velocity for both of the TiO_2 types as compared to fluidization that employed only vibration assistance. Additional experiments were performed with the MVA to characterize the synergistic effects of vibrational intensity and gas velocity on the TiO_2 P25 and P90 fluidized bed heights. Mathematical relationships were developed to correlate vibrational intensity, gas velocity, and fluidized bed height in the MVA. The non-dimensional bed height in the MVA system is comparable to previously published P25 TiO_2 fluidization work that employed an alcohol in order to minimize the electrostatic attractions within the bed. However, the MVA system achieved similar results without the addition of a chemical, thereby expanding the potential chemical reaction engineering and environmental remediation opportunities for fluidized nanoparticle systems.

In order to aid future scaling up of the MVA process, the agglomerate size distribution in the MVA system was predicted by utilizing a force balance model coupled with a two-fluid model (TFM) simulation. The particle agglomerate size that was predicted using the computer simulation was validated with experimental data and found to be in good agreement.

Lastly, in order to demonstrate the utility of the MVA system in an air revitalization application, the capture of CO_2 was examined. CO_2 breakthrough time and adsorption capacities were tested in the MVA system and compared to a vibrating fluidized bed (VFB) system. Experimental results showed that the improved fluidity in the MVA system enhanced CO_2 adsorption capacity.

TABLE OF CONTENTS

CHAPTER Page

CHAPTER Page

LIST OF TABLES

Table Page

LIST OF FIGURES

Figure Page

Figure Page

Figure Page

Figure Page

1. INTRODUCTION

1.1 Overview

Fluidization is broadly used in many industries for dispersing nanosized particles in a gas phase, due to the enhanced availability of surface area per unit mass of nanoparticles as compared to larger particles. Multiphase flow techniques (e.g. the fluidization of particles in a gas) are widely applied, including in chemical reaction systems, solids separations, fluidized bed combustion, heat/mass transfer or interface modification, and surface coatings. The list of fluidized bed applications is long. One example is the use of fluidized bed systems in industrial CO_2 capture in fluidized reactors such as with a post-combustion chemical looping process. Granite et al. [1] used a chemical looping combustion method to reduce CO_2 emissions. In this process, enhancing the contact efficiency between the gases and solid particles is essential since the particles chemically interact with the gas phase in the fluidized bed. Understanding the flow characteristic and physical properties of fine particles is essential when designing and operating a fluidization system. Despite the expanded interest in the fluidization of particles for environmental remediation, there are challenges that exist with the fluidization of very fine powders. The presence of numerous nanosized particles leads to the formation of large agglomerates due to the large interparticle forces (e.g. electrostatic and Van der Waals forces) [2]. When using nanosized powders, particularly agglomerate bubbling fluidization (ABF) types of particles, the fluidization is described by exceptionally restricted bed expansion and large bubble formation when the minimum fluidization velocity is attained [3].

Several studies were carried out to investigate the effects of vibration on particle fluidization. Barletta at el. [4] studied the fluidization behavior of a fine aeratable powder assisted by mechanical vibration in a reactor. The investigated parameters of vibration were the vibrational intensity (a/g = 0.5, 1 and 2) and the frequency (between 7 and 200 Hz). The vibrational acceleration, a, is related to the sinusoidal displacement due to vibration, and g is gravitational acceleration. The largest effects on bed expansion and differential pressure drops were found at low frequencies close to the natural frequency. Valverde et al. [5] studied fine and ultra-fine powders in centrifugal fluidized beds (CFB) and vibro-fluidized beds (VFB). Experiments performed in the VFB showed that the quality of fluidization was improved with increased acceleration. Zhou et al. [6] adopted a vibrated dense medium fluidized bed (VDMFB) to remove noncombustible impurity minerals for fine coal separation. As the vibration frequency increased to a level close to the fluidized bed's natural frequency, the minimum fluidization velocity decreased significantly.

The work presented in this thesis is a larger project focused on understanding the dynamics of nanoparticle behavior in a new fluidization system, simulation of fluidization dynamics, and application of the novel fluidized bed system to improve CO_2 capture capacity. The understanding of fluidized agglomerate formation, behavior, and size is important in order to improve the quality of nanoparticle fluidization and its applications.

1.2 Statement of Problem

The major challenge with past work was that several studies utilized chemicals such as

alcohols to minimize the electrostatic forces in the fluidized bed systems that were used [7-9]. The addition of an alcohol vapor to a system that employs a photocatalyst such as TiO_2 significantly reduces the particle-to-particle and particle-to-reactor surface electrostatic charges, thereby improving fluidization quality [10]. However, the alcohol limits the use of a TiO_2 nanoparticle fluidization system for environmental remediation work due to the alcohol's interactions with and reactions on the surface.

Previously published work used computational simulations to examine the behavior of different fluidization systems. Kuipers et al. [11] studied the fluid dynamics of bubble shape and growth in a fluidized bed with the aid of a two-fluid model (TFM) in two-dimensional space. Pain et al [12] utilized a finite element method to analyze the fluidization dynamics based on the Kolmogorov entropy and the Lyapunov exponent in the transient fluidized bed simulation. Grid convergence tests were carried out in order to investigate the bubble size and shape using differing numerical resolution to quantify the similarities between experiment and simulation results. In general, a refined grid is necessary to achieve a reasonable bubbling behavior based on a grid convergence test. Souza et al. [13] analyzed the effect of diffusion in the convection terms and mesh sizing effect using the Eulerian-Eulerian two fluid model. The author stated that a higher order method was recommended for the diffusion term in order to obtain accurate results near high pressure gradient regions (e.g. shock waves) that generate numerical oscillations. Huilin et al. [14] investigated the motion of particles in a fluidized bed using the Eulerian-Eulerian two fluid method approach. The authors stated that it was important to examine the particle size distribution and energy dissipation in order to obtain stable behavior of the

fluidized bed. Goldschmitt et al.[15] worked on the effect of the coefficients of restitution using the kinetic theory of granular flow in the dense gas fluidized bed. They concluded that the dynamics of dense gas fluidized bed relies on particle to particle interaction and energy dissipation. Based on the previous studies, we could conclude that the dynamic modeling of a fluidized bed needs experimental data, specifically the behavior of the gas-solid fluidized bed and solid-solid interaction that relates to agglomeration during the fluidization process. A deep understanding of the interaction between the agglomerates in the fluidized bed is vital, since these interactions affect the dynamic behavior of the particles and, if used for chemical reactions, the conversion of the chemical species in the bed.

1.3 Contributions

The work described in this dissertation was aimed at developing a nanoparticle fluidization system that may be useful for a wide range of applications where fluidization is needed in a relatively pristine matrix (i.e. in the absence of an alcohol). A microjet and vibration assisted (MVA) fluidized bed was developed. The MVA system is, as of the writing of this dissertation, a patent-pending technology by the Andino research group at Arizona State University [16].

The thesis is divided into two main sections: the design of the new system and the testing of the system in an environmental remediation application. The work that was undertaken employed nanosized titanium dioxide (TiO_2), an ABF type particle, as the test particle due

to its usefulness in air pollution control applications. Photocatalytic TiO_2 surfaces are activated for chemical reactions when light of a sufficient energy reaches the surface. Reaction on the surface is enhanced when the compounds of interest are able to adsorb to the surface through the availability of more surface area (on a per volume basis) with smaller sized particles as compared to larger particles. Both properties that are needed to enhance the use of a photocatalyst in air purification can potentially be achieved through the fluidization of nanoparticles. The operating conditions of the MVA system were optimized, and the system was subsequently applied to enhance CO_2 capture efficiency on the TiO_2 nanoparticles. The subject of CO_2 conversion using oxide materials is an ongoing theme within the Andino Research Group at ASU [17-22] that would benefit from enhanced capture of CO_2 on oxide materials in a continuously flowing system. It was hypothesized that the higher fluidized bed height that could be achieved by the novel MVA system would correspond to improvements in the CO_2 capture efficiency. The actual CO_2 concentrations were measured at the outflow of the fluidized bed system. Results from the MVA system were compared to a simple vibrating fluidized bed (VFB) to examine the impact of bed height on CO_2 capture.

For the first time, we have designed a system and studied the dual effects of vibration and a downward microjet on the fluidization of nanosized TiO_2. This new method with unprecedented microjet and vibration assisted (MVA) fluidization is expected to overcome the problem of agglomeration of the ABF powder in the absence of an alcohol solution. The fluidization quality, as measured by the parameters of nondimensional bed height, nondimensional pressure drop, and minimum fluidization velocity were determined.

2. DEVELOPMENT OF THE MICROJET AND VIBRATION ASSISTED FLUIDIZATION SYSTEM: EXPERIMENTAL

Note that a portion of this chapter is the subject of a published paper: An, K. and Andino, J. M., (2019) Powder Technology 356, 200-207.

2.1 Introduction

The fluidization behavior and dynamics of nanoparticles in gases are complex as compared to larger powders. Significant elutriation with large bubble and channel formation can be observed when nanoparticles are fluidized using a high superficial velocity. Thus, the objective of this research is to develop a novel and efficient method that can be applied to enhance the fluidization quality of nanoparticles in order to expand the potential applications of fluidized nanoparticle systems.

Quevedo et al. [23] studied microjet assisted fluidization using agglomerate particulate fluidization (APF) and ABF type nanosized powders. They found that the quality of gas-solid fluidization of nanoparticles was greatly enhanced by adding a high-velocity jet produced by a micronozzle pointing vertically downward. Use of an APF type nanopowder expanded the bed by up to 50 times its original bed height, and difficult-to-fluidize agglomerate bubbling fluidization (ABF) type nanopowders exhibited behavior similar to the APF type, although with lower bed height expansion. Pfeffer et al. [24] used a microjet to enhance the fluidization of nanoparticles and agglomerates. The turbulent flow created by the microjet was advantageous for fluidizing the agglomerates, and the shear generated

by the microjet was effective in breaking apart the agglomerates. Wang et al. [25] investigated the flow behavior of gases and particles in a cylindrical fluidized bed for different jet velocities through a two-fluid model simulation. The air jet penetration length was discussed and showed good agreement between the numerical simulations and experimental results.

In this work, a new method for enhancing the fluidization of nanoparticles was developed. The method is based on the use of a downward-pointing micronozzle and vibration to enhance the quality of nanoparticle fluidization. The use of a downward micronozzle as a secondary flow in addition to the magnetic vibrator, was hypothesized to enhance bed expansion and suppress the onset of bubble and channel formation due to the enhanced dispersion of the powder.

2.2 Experimental Setup

2.2.1 Apparatus and Operating Conditions

The experiments were performed in a custom-designed column reactor with an inner diameter of 76 mm and a height of 800mm made of clear cast acrylic. Martin et al. [26] emphasized the point that fluidized bed scaling may influence performance. Thus, the current work matched the lab-scale reactor dimensions to previous work [23] in order to provide initial comparisons before further enhancing the system. Nanosized powders were fluidized with high purity nitrogen at a superficial velocity range from 0.005 to 0.035 m/s, supplied to the bottom of the fluidized bed through a gas distributor consisting of a sintered

quartz plate 2mm thick having a pore size of 20 microns. The nitrogen from the compressed gas cylinder was humidified by being passed through a water bubbler that connected to the bottom of the column. The exhaust gas from the bed was filtered through a HEPA filter to trap any elutriated nanoparticles. The pressure drop was measured using a differential pressure manometer (RISEPRO HT-1890) between two taps, one at the top of the column and the other located 2 cm above the gas distributor. The transparent bed reactor was mounted on a custom-made wooden plate with four springs attached to it in order to isolate the vibrational motion from the lab bench surface and the ground. An electromagnetic vibrator was mounted below the wooden plate that supported the transparent bed reactor. Electromagnetic vibration was controlled by a signal generator (Cleveland Vibrator Co. VAF-3) which provided vertical sinusoidal motions with controlled amplitude and frequency. The frequency range that was used was from 40 to 70 Hz, and the amplitude was monitored using a vibration meter (PCE Instruments #PCE-VT 2700) that was attached to the table. Initial experiments were conducted to determine the resonant and anti-resonant frequencies for the system since these are critical parameters for vibrating systems [27,28]. The downward pointing nozzle was placed at a height of 10 cm above the distributor since this placement previously showed enhanced fluidization performance in a system with identical dimensions [29-34]. The micronozzle was connected to a pressure regulator that was used to generate the secondary flow. The nozzle diameter used in this work was 500 microns, which is identical to the nozzle size used by Quevedo et al. [23] The

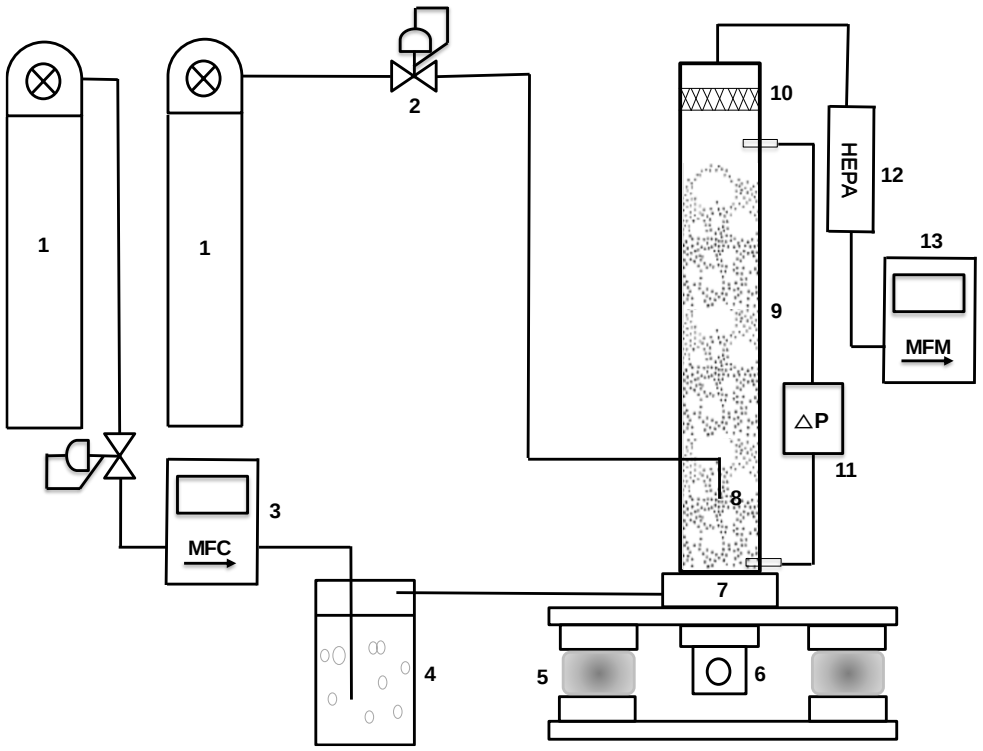

Figure 1: Schematic of the System. Key: 1: Compressed N_2 Cylinder, 2: Pressure Regulator, 3: Mass Flow Controller, 4: Water Bubbler, 5: Vibration Isolator, 6: Magnetic Vibrator, 7: Gas Distributor 8: Micronozzle, 9: Fluidization Reactor,10: Pre-Filter, 11: Pressure Manometer, 12: HEPA Filter, 13: Mass Flow Meter

overall schematic of the experimental setup is shown in Fig. 1.

Dry nitrogen was supplied from a compressed gas cylinder and subsequently humidified by passing the nitrogen through a water bubbler. A mass flow controller (MFC) was used to control the gas flow rate at the bottom distributor, as shown in Fig. 1. The mass flow controller had a range from 0 to 15 L/min to enable adjustment of the superficial velocity through the reactor. Two pressure regulators were used to produce flow through the micronozzle at 5 psig and gas flow through the mass flow controller. The absolute pressure ratio ($P_{downstream}/P_{upstream}$) across the micronozzle in the MVA system was 0.746, different

than the critical pressure ratio of 0.52 which is required to achieve choked, sonic flow [35].

In order to compare our results to those that were obtained previously [23], we conducted background experiments using commercial TiO_2 nanosized powders. We employed simple microjet assisted (MA) fluidization as well as a vibro-fluidized bed (VFB) in the absence of an alcohol. Quevedo et al. [23] used a microjet as a secondary flow to the superficial flow with a dilute alcohol solution to break-up large agglomerates, prevent channeling, bubbling, and promote liquid-like fluidization. Our experiments using a combined microjet and vibration assisted (MVA) fluidization in the absence of an alcohol solution were compared with simple MA and VFB fluidization in the absence of an alcohol as well as the previously published results of MA with an alcohol support.

The optimal experimental conditions of the MVA and VFB systems were investigated by examining the nondimensional bed height, nondimensional pressure drop, and minimum fluidization velocity. The experiments were performed under different conditions. First, we varied the vibrational frequency (40 Hz to 70 Hz) and vibrational intensity (1 to 2) while the superficial gas velocity (0.02 m/s) was held constant. Additionally, we examined the MVA system's nondimensional height versus vibrational frequency (40 to 70 Hz) for both powders with two different superficial gas velocities (U_g) of 0.01 and 0.02 m/s to find the optimal condition of vibration in the MVA system. Secondly, we performed the experiments by varying the superficial gas velocity (0.005 to 0.035 m/s) and maintaining a constant vibrational intensity and frequency (using the optimal vibration parameters determined in the first set of experiments) to check the effect of the superficial velocity on the fluidized bed. Thirdly, three dimensional plots were created to show the synergistic

Table 1. Experimental Conditions

Powder Mass [g]	50
Vibrational Frequency [Hz]	40, 50, 60, 70
Vibrational Intensity	1, 1.2, 1.4, 1.6, 1.8, 2.0
Gas velocity [m/s]	0.005 to 0.035

effects of the vibrational intensity and superficial gas velocity on bed expansion. Lastly, the nondimensional pressure drop was examined as a function of superficial gas velocity to determine the

minimum fluidization velocity for both the VFB and MVA systems. The characteristics of fluidization were investigated by increasing the superficial gas velocity in small steps (0.1 cm/s), starting from 0.005 m/s. The vibrational intensity range was determined by the vibratory system's frequency and amplitude range based on its operating conditions.

For the MVA system, the fluidized bed height expansion ratio (the nondimensional height) and the bed pressure drop were recorded while the vibrator was turned on. In all cases where MVA fluidization was employed, the vibrator was turned on before the microjet was started in order to avoid large bubble and channel formation. The fluidized bed behavior as well as the pressure drop value stabilized after 1 minute with the optimal condition. The minimum fluidization velocity (U_{mf}) was determined by a plot of nondimensional pressure drop against the gas velocity. The operating conditions of all fluidization experiments are shown in Table 1.

Table 2. Material Properties of TiO_2 Nanopowders

Material	Brand/Manufacturer	Primary Particle Size [nm]	Surface Area $[m^2/g]$	Tap Density $[kg/m^3]$
TiO_2 P25	Aeroxide/ Evonik-Degussa	21	50	130
TiO_2 P90	Aeroxide/ Evonik-Degussa	14	90	120

2.2.2 Materials

Two agglomerate bubbling fluidization (ABF) type nanopowders were used: TiO_2 P25 and TiO_2 P90 manufactured by Evonik-Degussa [36]. Before all experiments, the nanopowder was sieved using a 500 μm sieve placed on a vibration shaker, in order to remove large agglomerates that may have formed during storage. The properties of TiO_2 P25 and P90 are shown in Table 2. The tap densities for P25 and P90 were validated using tap density tester (SDTAX TD1).

2.3 Results and Discussion

The relationship between amplitude and vibrational frequency for the system was investigated and the results are shown in Fig. 2. The data suggest that the resonant and anti-resonant frequencies are, respectively, 50 and 60 Hz.

Baseline background studies using just a microjet in the absence of an alcohol to minimize

electro-static effects resulted in poor fluidization. As seen in Fig. 3, using only microjet assistance to fluidize the TiO_2 P25 particles in the absence of an alcohol and under nonchoked flow conditions led to severe channeling and powder fluctuation problems. This result showed the need for additional fluidization assistance methods (e.g. vibration) for TiO_2 nanosized powders.

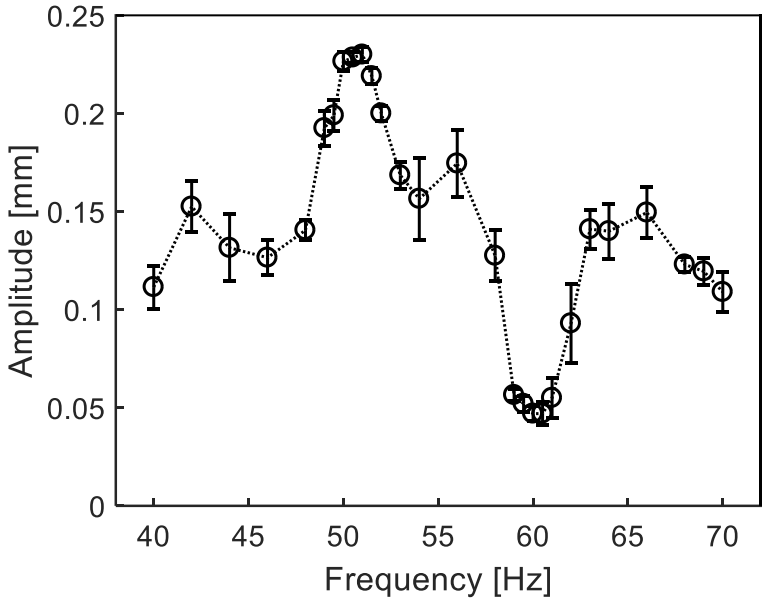

Figure 2. Amplitude versus Frequency Domain of the Experimental Setup. Data Points for this Figure are included in Appendix A, Table A.1.

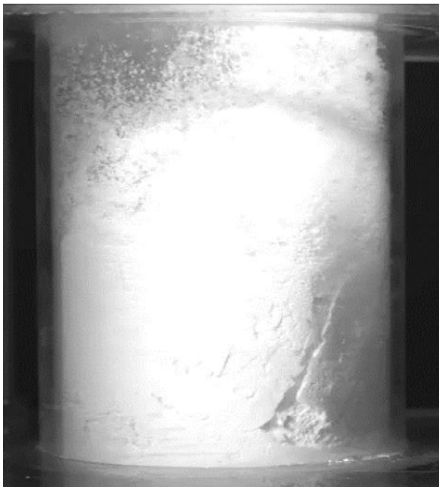

Figure 3. Microjet Assisted (MA) Fluidized Bed Channeling (without Alcohol Support)

2.3.1 Bed Expansion Behavior, Influence of Vibration

The experimental results of the MVA fluidized bed that appear in Fig. 4 show the evolution of the nondimensional height of the fluidized bed against the vibration intensity range from 1 to 2 with vibrational frequencies of 50, 60 and 70 Hz. Fig. 4 (a) and (b) represent TiO_2 P25 and TiO_2 P90 nanopowder, respectively. Nondimensional bed height (H_{nd}) was obtained by dividing the stable fluidized bed height by the initial packed bed height when the sieved TiO_2 powder had been just loaded, and is described by Equation 1:

$$H_{\text{nondimensional (nd)}} = H/H_0 \qquad \text{(Equation 1)}$$

where: H = the stable fluidized bed height

H_0 = initial packed bed height.

Multiple readings were taken at each experimental condition's bed height to confirm the measurements, and error bars represent the overall distribution of the data. The vibration

intensity (Γ) is defined as the ratio of vibrational acceleration to gravitational acceleration, and can be described mathematically by Equation 2 [37-39]:

$$\Gamma = (A w^2)/g \qquad \text{(Equation 2)}$$

where: A is the amplitude of vibration, as adjusted and measured by vibration meter

$w = 2\pi f$

f = the frequency in Hz, as set with the signal controller

g = gravitational acceleration, 9.8 m/s^2.

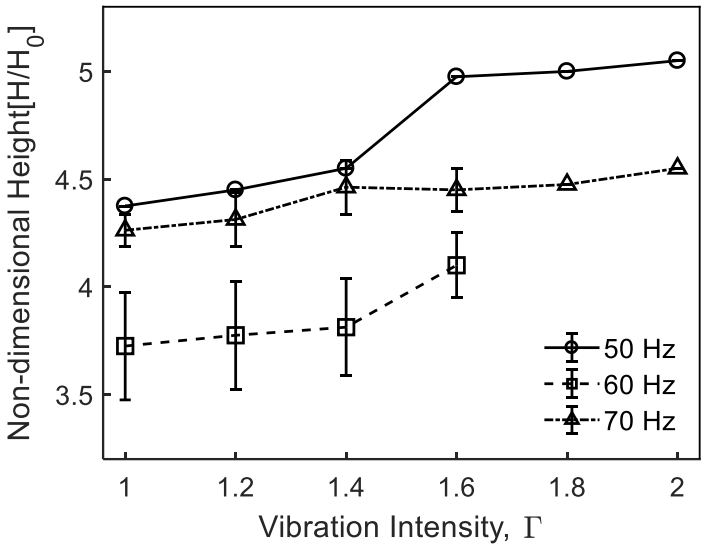

(a)

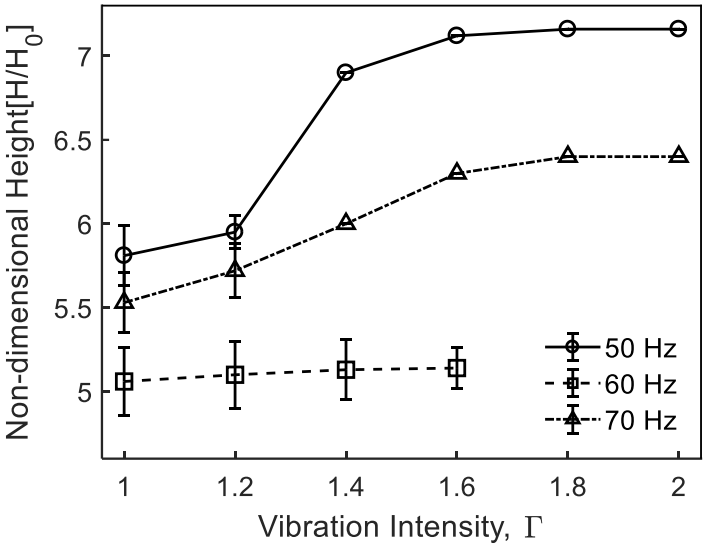

(b)

Figure 4. Nondimensional Height as a Function of Vibration Intensity at Different Frequencies, 50, 60 and 70 Hz in the MVA System. The Plots are for (a) TiO_2 P25 and (b) TiO_2 P90 Nanopowders. Data Points for these Figures are included in Appendix A, Table A.2.

From Fig. 4, the nondimensional height was the largest with a vibration intensity of 50 Hz, the resonant frequency for both TiO_2 P25 and TiO_2 P90 powders in the custom-

designed system that was used. For the TiO_2 P25 powder, the nondimensional height increased up to a stable value of 5 when the vibration intensity was 1.6. The nondimensional bed heights for both TiO_2 P25 and P90 were the smallest at a frequency 60 Hz with all intensity ranges that were tested. The MVA fluidized bed height decreased significantly at the antiresonance frequency at 60 Hz and showed the maximum nondimensional height at 50 Hz, the resonance frequency. Nevertheless, the current work shows that, for TiO_2 powders, vibration with adjusted frequency and amplitude improves the fluidization quality (as measured by the nondimensional bed height) by supporting the gas flow to overcome interparticle forces and break up channels. It is important to note that only limited data at a vibrational frequency of 60 Hz were acquired because of an exceptionally small amplitude since 60 Hz corresponded to the antiresonance frequency of the system, as shown in the data that appear in Fig. 2. Fig. 5 shows the nondimensional

height versus vibrational frequency from 40 to 70 Hz for both powders, TiO_2 P25 and P90 at superficial gas velocities (U_g)

of 0.01 and 0.02 m/s. Once again, a higher nondimensional height was observed for TiO_2 P90 as compared to P25. As can be seen from Fig. 5, the maximum nondimensional height can be found at a frequency of 50 Hz and a gas velocity of 0.02 m/s. Thus, it can be concluded that the TiO_2 particle properties such as smaller primary particle size and lower tap density for P90 as compared to P25 significantly affect the nondimensional height result.

2.3.2 Influence of Superficial Gas Velocity

As seen in Fig. 6, when increasing the superficial gas velocity under a fixed vibrational frequency of 50 Hz and vibration intensity of 1.6, the non-dimensional height of TiO_2 P25 increased and then stabilized. The maximum bed expansion of the MVA fluidized Aeroxide TiO_2 P25 was approximately 5 times the initial bed height. The MVA fluidized

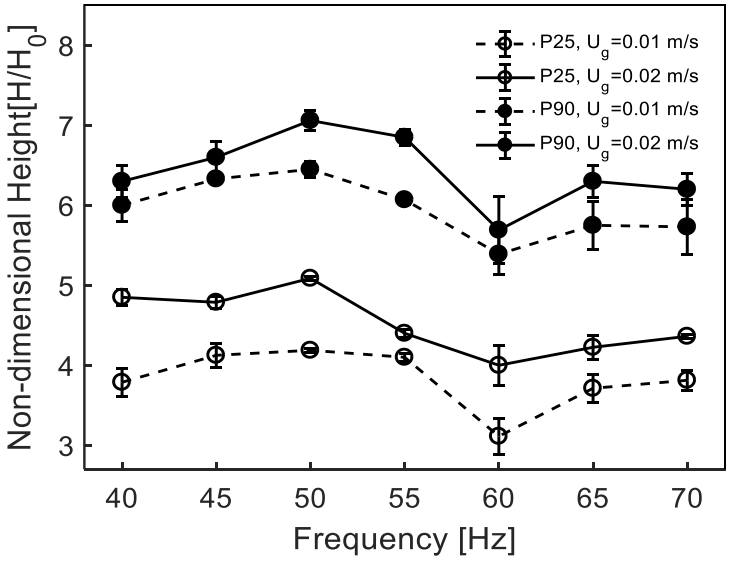

Figure 5. Nondimensional Height as a Function of Frequency at Different Gas Velocities (Vibrational Intensity: 1.6, Vibrational Frequency: 50 Hz). Data Points for this Figure are included in Appendix A, Table A.3.

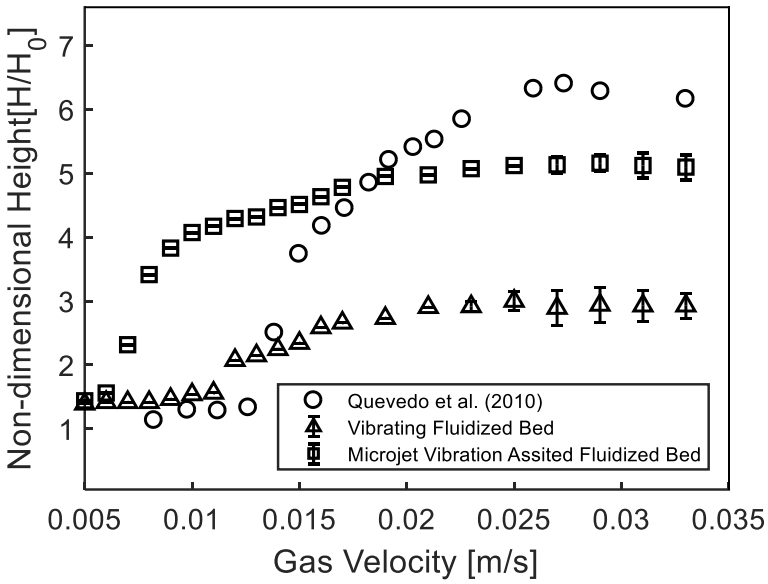

Figure 6. Nondimensional Height of TiO_2 P25 as a Function of Superficial Gas Velocity for a Frequency of 50 Hz and a Vibrational Intensity of 1.6. Data Points for this Figure are included in Appendix A, Table A.4.

bed height did not expand further, and the bed height remained constant when the superficial gas velocity reached 0.017 m/s. It is important to note that the nondimensional bed height for TiO_2 P25 in the MVA fluidized bed system was similar to the previously published nondimensional bed height that was obtained in a similar system that used microjet assisted (MA) fluidization but employed an alcohol solution. [23] The current result is significant in terms of photocatalytic air purification, since a chemical did not have to be introduced in order to achieve similar bed expansion results that would be beneficial for gas-surface reactions. Also, it was observed that vibration assisted fluidization (VFB) alone resulted in only a bed expansion of 3 times the initial TiO_2 P25 bed height. In addition, the VFB system showed some fluctuation at the top of the bed when the gas velocity was greater than 0.023 m/s, suggesting a strongly turbulent regime for gas velocities of 0.023 m/s or greater. Thus, the VFB system was less efficient in fluidizing the nanopowders as compared to the MVA

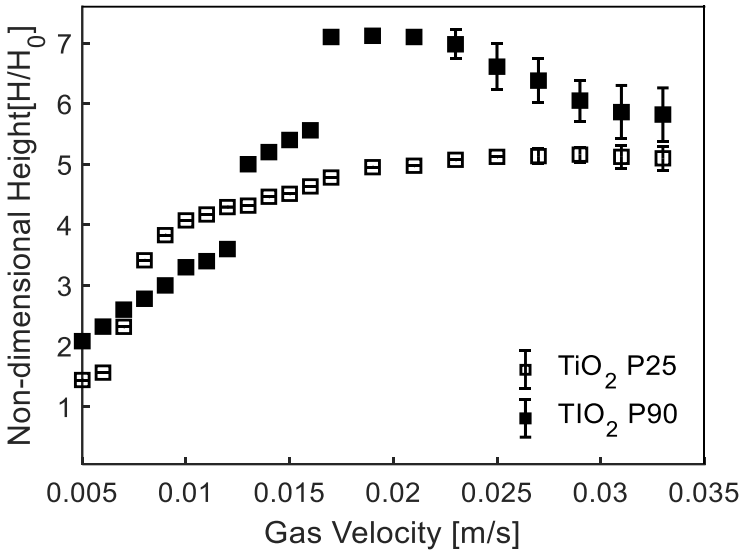

Figure 7. Nondimensional Height as a Function of Gas Velocity in the MVA System for TiO_2 P25 and TiO_2 P90 Nanopowders. Data Points for this Figure are included in Appendix A, Table A.5.

system. Fig. 7 shows the comparison of nondimensional height as a function of superficial gas velocity for TiO_2 P25 and TiO_2 P90 nanopowders in the MVA system. The nondimensional height obtained using TiO_2 P90 (H_{nd} of 7) is higher than that obtained using TiO_2 P25 (H_{nd} of 5) at about gas velocity 0.02 m/s because of the smaller density and primary particle size of TiO_2 P90 as compared to TiO_2 P25. However, the nondimensional height of the TiO_2 P90 bed decreased after a gas velocity of 0.023 m/s, and a large fluctuation was observed at the top of the fluidized bed. The flow profile in the fluidized bed was in a strongly turbulence regime above a gas velocity 0.023 m/s.

In order to employ fluidization as a tool in environmental remediation efforts, the system must be stable over time. Fig. 8 shows the evolution of the MVA system's nondimensional bed height as a function of the fluidization time. The fluidized bed heights increased up to maximum after a short time for both TiO_2 nanopowders and remained constant for the

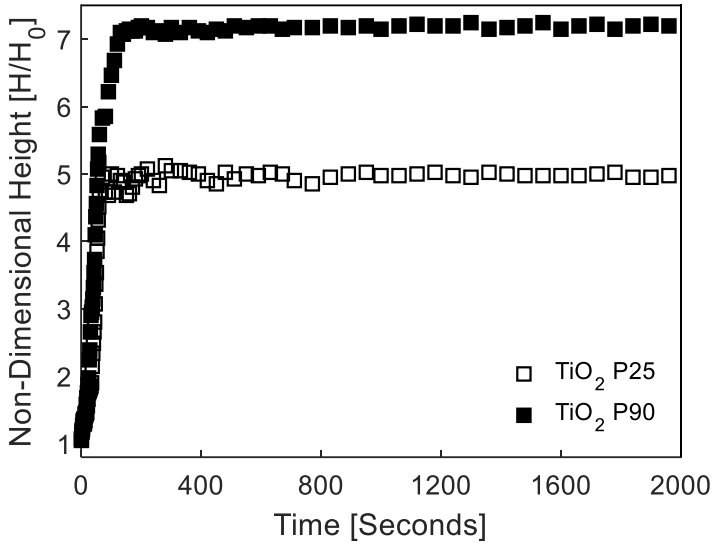

Figure 8. Nondimensional Height as a Function of Fluidization Time P25 and P90 TiO_2. (Gas Velocity: 0.02 m/s, Vibrational Intensity: 1.6, Vibrational Frequency: 50 Hz)
Data Points for this Figure are included in Appendix A, Table A.6.

entire testing time of 2000 seconds (33.3 minutes). This experimental result indicates that the MVA system has the potential to be applied to systems that are needed for continuous air purification processes. Longer testing times are needed, but it is important to conduct this work when specific chemical reactions, yields of products, and the influences of the formed products can also be simultaneously assessed.

2.3.3 Influence of Upstream Pressure

In this work, the pressure upstream of the 500 μm micronozzle was varied between 5 and 30 psig to show the influence of microjet assistance on the bed height. Theoretically, the flow through the micronozzle is said to be choked at pressures greater than 15 psig upstream, with a surrounding atmospheric pressure. Fig. 9 shows the experimental results of choked flow at 15 psig upstream pressure fed to the 500 μm micronozzle in the MVA

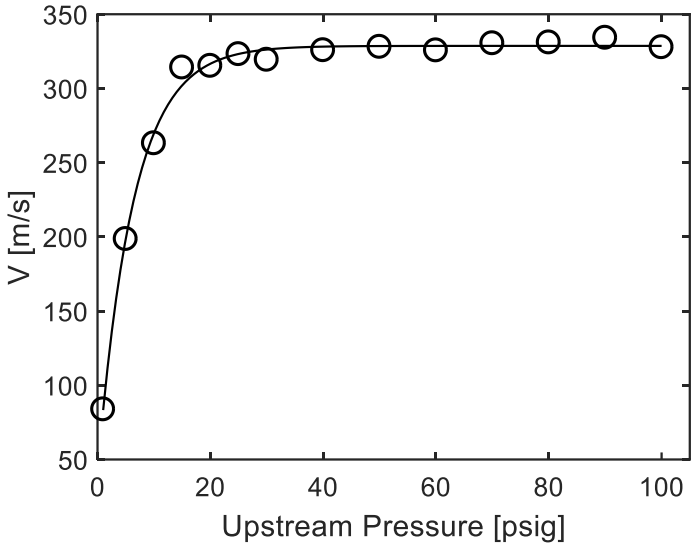

Figure 9. Experimental Result of Outlet Velocity of the Micronozzle at Different Upstream Pressures. Data Points for this Figure are included in Appendix A, Table A.7.

system. The resulting flow through the micronozzle becomes sonic if we assume adiabatic, frictionless, compressible flow of nitrogen [40].

We performed the experiments under the conditions as shown in Table 1. Fig. 10 shows the nondimensional height profile as a function of vibrational intensity at different upstream pressures of nitrogen that were fed into the micronozzle. When the gas velocity and the vibrational frequency reached 0.02 m/s and 50 Hz, respectively, the nondimensional height reached its maximum. Although not shown in Fig. 10, it is important to note that when the vibrational frequency was fixed at other frequencies (e.g. 60Hz, the anti-resonance frequency) the fluidization was more unstable and the bed expansion ratio decreased. As seen in Fig. 10, higher pressures caused variation in the bed height due to excessive flow from the microjet. This is illustrated in the error bars that are

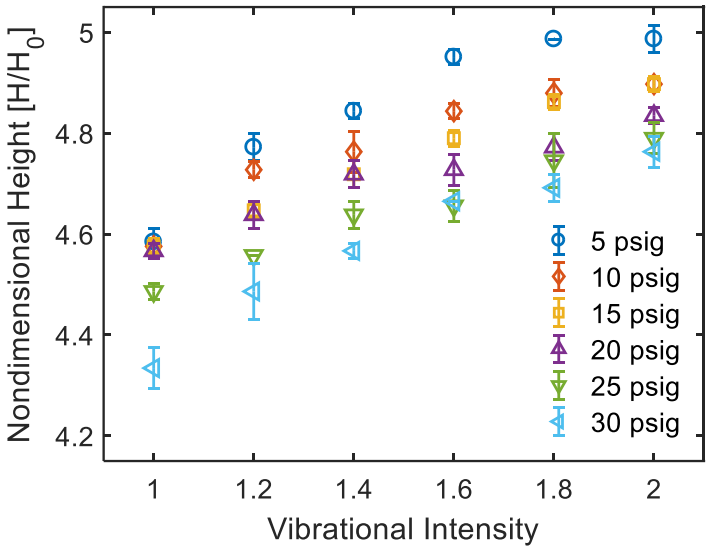

Figure 10. Nondimensional Height of TiO_2 P25 Powder as a Function of Vibrational Intensity at Different Upstream Pressures through the Microjet (Frequency: 50 Hz). Data Points for this Figure are included in Appendix A, Table A.8.

included with the data points in Fig. 10. The results indicate that the MVA system achieved higher nondimensional heights using lower upstream pressures (and hence lower micronozzle flow rates). However, when the micronozzle flow was completely turned off, the nondimensional height went down to 2.5, as shown in Fig. 6. Quevedo et al. [24] employed a similarly sized micronozzle as in the current work, but employed an alcohol solution and a nitrogen gas pressure through the micronozzle of 20 psig (sonic flow condition). They achieved stable fluidization with expanded beds up to 6 times the original bed height. The results in Fig. 9 and Fig. 10, indicate that subsonic velocity through the micronozzle was sufficient in the MVA system to achieve fluidization (and preferred in terms of enhancing the bed expansion in the absence of alcohol support) due to the added vibrational assistance. This result is particularly significant in terms of enabling more

applications that would benefit from nanoparticle fluidization but where relatively pristine chemical conditions are required.

2.3.4 Synergistic Effect of Vibration and Superficial Gas Velocity

A 3-Dimensional surface fit (2^{nd} order polynomial) has been proposed to describe the synergistic effect of the vibrational intensity and superficial gas velocity on the nondimensional height of the fluidized bed, as shown in Fig. 11. A total of 155 experimental data points per TiO_2 powder type at different conditions were obtained. The mechanical vibration and microjet assistance imposed on the bed allows for the transfer of energy through particle-to-particle collisions, thus enhancing the bed height. As shown in Fig. 11(a) and (b), the nondimensional bed heights of TiO_2 P25 and P90 increased gradually up to their maximum values of 5 and 7, respectively, when both the vibrational intensities and gas velocities increased. After a gas velocity of 0.02 m/s and a vibrational intensity of 1.6, the nondimensional height of TiO_2 P25 reached a plateau. The nondimensional height of TiO_2 P90 powder was higher, suggesting more fluidic behavior than TiO_2 P25 due to its particle properties (see Table 2). To further test the mathematical model that was developed and verify the surface fitting curve, 18 additional sample points, i.e. 9 unique gas velocity/vibrational intensity conditions each

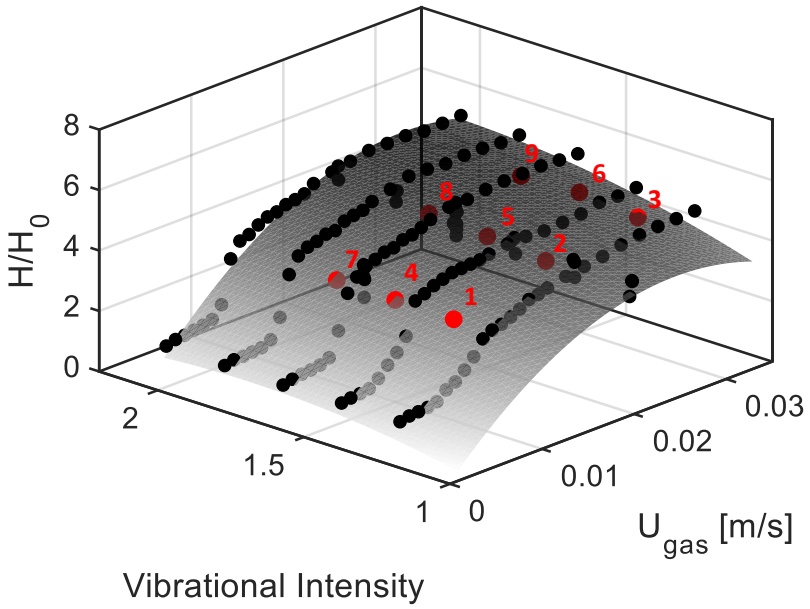

(a)

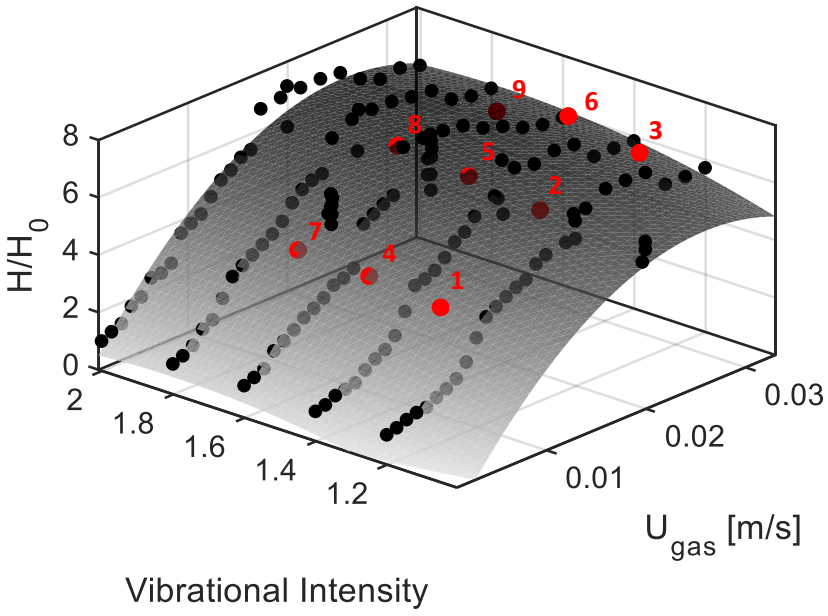

(b)

Figure 11. 3-Dimensional Surface Fit to show the Synergistic Effect of Vibrational Intensity and Superficial Gas Velocity on Nondimensional Height: (a) TiO_2 P25, (b) TiO_2 P90. (The 9 Red dots are Sampling Points to compare with the Nondimensional Height that is predicted by the 2nd Order Polynomial Surface Fit). Data Points for this Figure are included in Appendix A, Table A.9 & A.10.

for P25 and P90 TiO_2were tested and compared with the 2nd order polynomial model. The nine datapoints were for gas velocities of 0.01, 0.02, 0.03 m/s and the vibrational intensity at 1.3, 1.5, 1.7. Fig. 12 depicts the percentage error between the experimental and model predictions of the non-dimensional bed heights for the additional sample points for the two powders. Fig 10 indicated less than 14% error between the actual and calculated non-dimensional bed heights for TiO_2 P25 and less than 7.8% for TiO_2 P90. The largest error appeared at the experimental condition of large gas velocity (0.03 m/s) coupled with high vibrational intensity (1.7) due to the fluidized bed fluctuation from an excessive support energy from vibration and superficial gas velocity.

It is important to note that higher order surface models, e.g third, fourth, and fifth order polynomials for two variable systems, were applied to represent the data. Although the data could be adequately modeled with higher order polynomials, the applicable ranges for vibrational intensities and superficial gas velocities was small. In expanded ranges, the higher order models did not adequately represent the physical phenomena of the system. Specifically, the higher order models predicted sharp increases in non-dimensional bed heights at the extreme end points of the superficial gas velocity and vibrational intensity ranges. Thus, the second order polynomial was determined to be the more realistic model of the system.

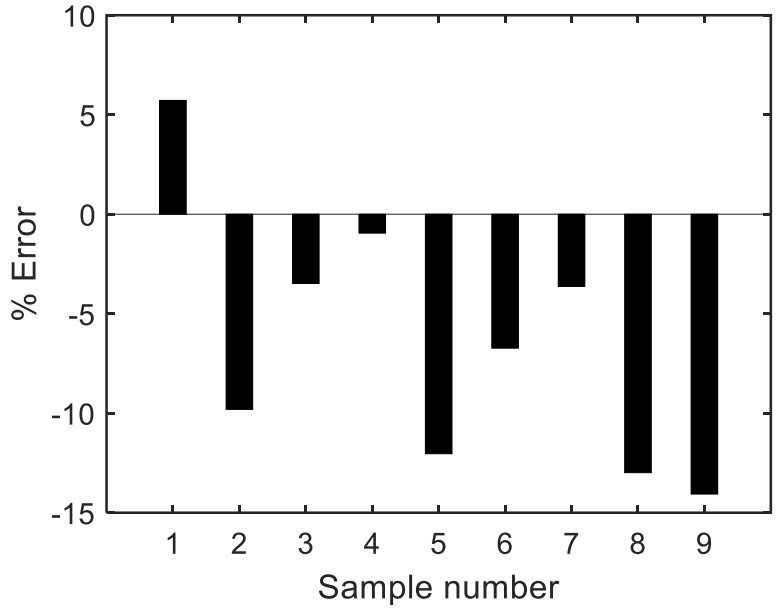

(a)

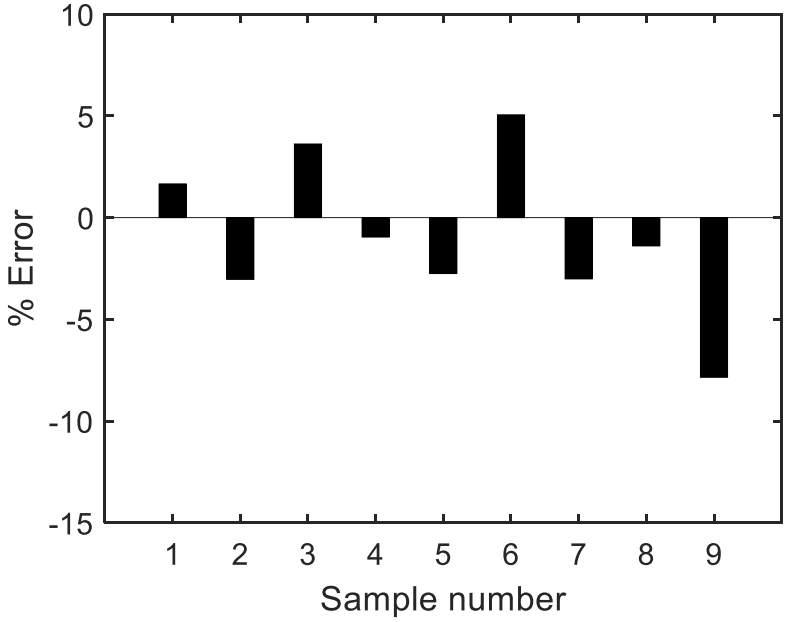

(b)

Figure 12. Error Percent from 9 Sampling Points: (a) TiO_2 P25, (b) TiO_2 P90. Data Points for this Figure are included in Appendix A, Table A.11.

2.4 Nondimensional Pressure Drop and Minimum Fluidization Velocity

The nondimensional pressure drop parameter is useful in indicating whether the gas flow suspends a portion of the powder's mass, and is another measure of the fluidization quality. A nondimensional pressure drop close to unity suggests that the flow suspends most of the entire mass of the powder. The nondimensional pressure drop was obtained using Equation 3:

$$P_{nondimensional(nd)} = \triangle P / m_{app} \qquad \text{(Equation 3)}$$

where: $\triangle P$ = The actual measured pressure drop across the fluidized bed

m_{app} = apparent weight of the bed (=mg/A)

m = mass of powder, g

g = gravitational acceleration, m/s^2

A = cross-sectional area of the column, m^2

The nondimensional pressure drop represents the ratio between the actual pressure drop across the fluidized bed and mass of powder in the reactor. The nondimensional pressure drop parameters for (a) TiO_2 P25 and (b) TiO_2 P90 are plotted against gas velocities and appear in Fig. 13 for the VFB and MVA fluidization systems. The figure shows that when combined microjet and vibrational assistance are applied, the TiO_2 nanopowders are suspended in the gas phase more than in the VFB system since the measured pressure drop approaches close to the apparent weight of the powder. The minimum fluidization velocity (U_{mf}) is a key parameter related to the fluidized bed system's quality and can be determined using the data of Fig. 13. For TiO_2 P25

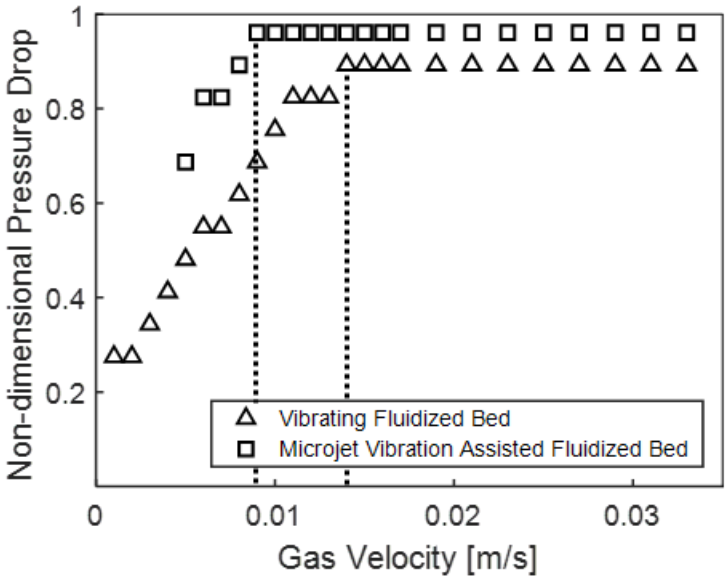

(a)

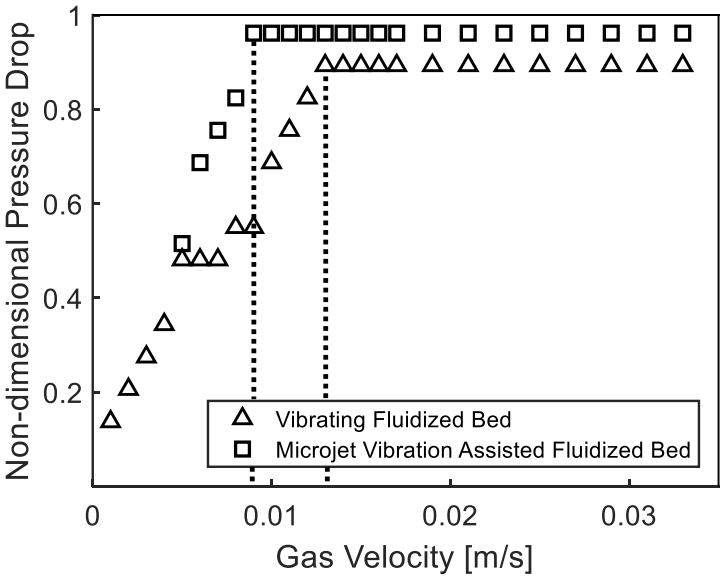

(b)

Figure 13. Nondimensional Pressure Drop as a function of Gas Velocity: (a) TiO_2 P25, (b) TiO_2 P90. Data Points for this Figure are included in Appendix A, Table A.12.

nanopowder, the minimum fluidization velocity (defined as the velocity where the pressure drop becomes constant) of 0.009 m/s for the MVA system is lower than the 0.013 m/s for the VFB system. For TiO_2 P90 nanopowder, a minimum fluidization velocity of 0.009 m/s was obtained for the MVA system (i.e the same value as for the TiO_2 P25). A minimum fluidization value of 0.014m/s for TiO_2 P90 using the VFB system was slightly higher as compared to when TiO_2 P25 was used. In either case, MVA fluidization resulted in a lower minimum required gas velocity as compared to the VFB system, thus suggesting more efficient and higher quality fluidization.

3. DEVELOPMENT OF THE MICROJET AND VIBRATION ASSISTED FLUIDIZATION SYSTEM: COMPUTATIONAL SIMULATIONS COMPARED TO EXPERIMENTS

3.1 Introduction

Computational fluid dynamics (CFD) simulations are widely used to analyze the behaviors of fluidized bed reactors. There are many physical models for CFD predictions of multiphase flows. Two approaches that are frequently used to model the gas-solid multiphase flow are the Eulerian–Eulerian and Eulerian-Lagrangian methods. Two-fluid model (Eulerian–Eulerian) simulation of the gas-solid fluidized bed is less computational demanding as compared to the Lagrangian-Eulerian Discrete Element Method (DEM) simulation [41]. Especially for nanosized particles in a fluidized bed, the interfaces between gas-solid phases in dispersed flows is highly dynamical and chaotic due to the large number of particles. If the total number of particles involved in many practical flows is extremely large, it may be computationally expensive and challenging to simulate the motion of each particle. The approximation of the solid phase as a continuum allows for faster computational calculation time as compared to the Lagrangian method [42]. The essential concept of the two-fluid model (TFM) in the gas-solid fluidized bed is the modeling of two interpenetrating continua [43,44]. Hernández et al. [45,46] utilized a two-fluid model of gas-solid fluidized bed approach to provide the physical details of the macroscopic characteristics of visible bubbles in the rage of 1 to 5 centimeters. The local gas velocities and volume fraction in the fluidized bed system were analyzed using a PIV (Particle Image

Velocimetry) method and compared with the TFM simulation.

The experimental data that have been presented in previous sections of this dissertation show the benefits of the MVA system in enhancing the fluidization of nanoparticles by increasing the expansion of the particle bed. An important consideration is the mechanism associated with this enhancement in bed height. The forces that play a role in the fluidization of nanoparticles in the MVA system are drag, collision, and van der Waals forces. Fabre et al. [47] carried out fluidized bed experiments in a column reactor with a 4.5 cm square-structured reactor using TiO_2 T805, TiO_2 P25 and Al_2O_3.They compared the forces as a function of the agglomerate size, showing that the dominant forces acting on the fluidized agglomerate of TiO_2 P25 were van der Waals and collision forces. We hypothesize that the MVA system amplifies the separation forces through the assistance of the microjet and vibration with constant van der Waals force that is the main force holding the agglomerates together, independent of gas velocity and particle diameter.

Simulations using the open-source multiphase software (from National Energy Technology Laboratory), MFiX version 19.2.0, employing a two fluid mdel (TFM) were carried out to provide information on the changes in the gas-phase velocity profile and particle sizes in the MVA system. These data were compared to available data from experiments. It was hypothesized that the MVA system contributed to the maintenance of small particle sizes (i.e. the minimization of agglomeration) and the minimization of the effects of electrostatic forces, thereby allowing for expanded bed heights.

Traditionally, two-fluid models have been used for simulating non-vibrating beds. In this work, a vibrational force and microjet assistance have been considered in the two fluid

model for the first time. The TFM model is based on the Navier-Stokes equations in which both the fluid and solids phases are treated as continua occupying the same cell in the simulation. Thus, it has two fluid dynamic equation sets, one for each phase, and additional equations are used to describe the interactions between the phases. For the solids phase, the solids pressure and viscosity were determined by the kinetic theory of granular flow (KTGF). Additionally, for the viscous stress model, the stresses are simple algebraic formulations of particle concentration and shear rate since it has been shown reasonably good predictions of velocity profiles in dense flow systems [48, 49]. For the frictional stress, the model has been used in a simpler formulation proposed by Schaeffer et al. [50,51]. Schaeffer and Pitman et al. [51] conducted a linear analysis of granular flow equations that included frictional stress terms and showed that the way the frictional stress is modeled influences the shape of the bubble and also the fluidized bed dynamics.

3.2 Equations of Two-fluid Simulation

The two-fluid method considers the two interpenetrating continuous phases, where one continuum refers to the gas phase in the bed and the other to the particle/solid phase. This concept allows the Eulerian-Eulerian description for both gas and solid phases without depending on the massive number of individual nano/micro-sized particles in the fluidized bed. The two-fluid method uses the general governing equations of conservation of momentum and mass for both the gas and solid phases. The momentum equation for the solid phase treats the solid as a fluid with transport properties (viscosity, diffusivity) based on the kinetic theory of granular flows [44]. There are displacements due to the vibration in the MVA fluidization system. These vibrations are expressed as a sinusoidal

displacement in the vertical direction. The sinusoidal displacement and the second derivative of the displacement can be formulated as shown in Equation 4 and 5:

$$\delta(t) = A_y sin(2\pi f t) \qquad \text{(Equation 4)}$$

$$\frac{\partial^2 \delta}{\partial t^2} = A_y 4\pi^2 f^2 (2\pi f t) \qquad \text{(Equation 5)}$$

where: δ= Sinusoidal vertical displacement due to vibration, mm

A_y= Amplitude in vertical direction, mm

f= Vibrational frequency, Hz

t= Time, seconds

The second derivative of the displacement is a vibrational acceleration term that acts as an apparent body force over both the gas and solid phases. As a result, the vibrational acceleration term could be implemented in the momentum balance equation for both phases as shown in Table. 3. As shown in Fig. 14, the constant gravity term will be replaced by an effective gravity, g_{eff}, to simulate a sinusoidally vibrating fluidized bed. Equation 6 shows the effective gravity where g is gravitational acceleration, 9.81 m/s^2.

$$g_{eff} = g - \frac{\partial^2 \delta}{\partial t^2} \qquad \text{(Equation 6)}$$

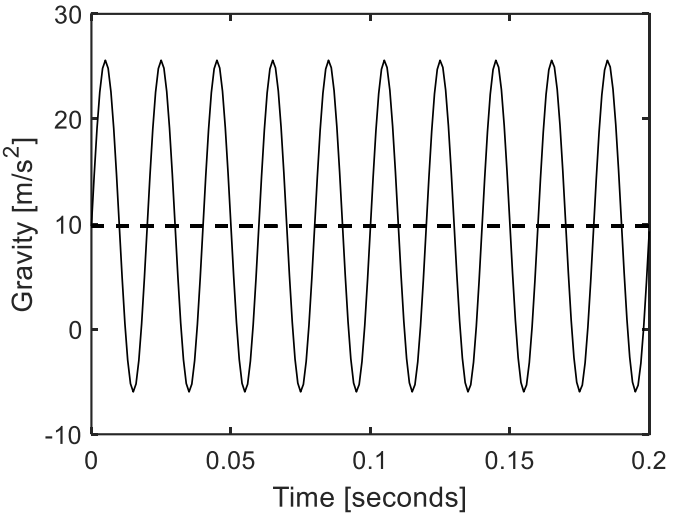

Figure 14. Effective Gravity as a Function of Time (f=50Hz, A_y=0.16 mm). The Solid Line represents the Sinusoidal Gravity due to the Vibration and the Dotted is Constant Gravity, g=9.81 m/s2.

The governing and closure equations [52] of the two-fluid model in 2D cartesian coordinates are shown in Equations 7-13

Equation of mass conservation for gas (g) and solid (s) phases

$$\frac{\partial}{\partial t}\left(\varepsilon_g \rho_g\right) + \nabla \cdot \left(\varepsilon_g \rho_g U_g\right) = 0 \qquad \text{(Equation 7)}$$

$$\frac{\partial}{\partial t}\left(\varepsilon_s \rho_s\right) + \nabla \cdot \left(\varepsilon_s \rho_s U_s\right) = 0 \qquad \text{(Equation 8)}$$

Equation of momentum conservation for gas and solid phases

$$\frac{\partial}{\partial t}\left(\varepsilon_g \rho_g U_g\right) + \nabla \cdot \left(\varepsilon_g \rho_g U_g U_g\right) = -\varepsilon_g \nabla P + \nabla \cdot \left(\varepsilon_g \tau_g\right) + I_{gs} + \varepsilon_g \rho_g \left(g - \frac{\partial^2 \delta}{\partial t^2}\right) \qquad \text{(Equation 9)}$$

$$\frac{\partial}{\partial t}\left(\varepsilon_s \rho_s U_s\right) + \nabla \cdot \left(\varepsilon_s \rho_s U_s U_s\right) = -\varepsilon_s \nabla P + \nabla P_p + \nabla \cdot \left(\varepsilon_s \tau_s\right) - I_{gs} + \varepsilon_s \rho_s \left(g - \frac{\partial^2 \delta}{\partial t^2}\right) \qquad \text{(Equation 10)}$$

Gas and solid phase momentum interface exchange

$$I_{gs} = K_{gs}(U_g - U_s) \qquad \text{(Equation 11)}$$

Drag coefficient between gas and solid phases

$$K_{gs} = \begin{cases} \frac{3}{4} C_D \frac{\rho_g \varepsilon_g \varepsilon_s |U_g - U_s|}{d_p} \varepsilon_g^{-2.65} & \varepsilon_g > 0.8 \\ 150 \frac{\varepsilon_s^2 \mu_g}{\varepsilon_g d_p^2} + 1.75 \frac{\varepsilon_s \rho_g |U_g - U_s|}{d_p} \varepsilon_g^{-2.65} & \varepsilon_g \leq 0.8 \end{cases} \quad \text{(Equation 12)}$$

$$C_D = \begin{cases} \frac{24}{Re}(1 + 0.15Re^{0.687}) & Re < 1000 \\ 0.44 & Re \geq 1000 \end{cases} \quad \text{(Equation 13)}$$

where: ε_g= Gas phase fraction

ε_s= Solid fraction

ρ_g= Gas phase density

ρ_s= Solid phase density

U_g= Gas phase velocity

U_s= Solid phase velocity

τ_g= Smallest mesh size

τ_s= Smallest mesh size

P_p= Particle pressure

I_{gs}= Inter-phase momentum exchange, kg/m^{2}s^2

K_{gs}= Gas-Solid momentum exchange coefficient, kg/m^{3}s

μ_g= Gas phase viscosity

In this work, the Eulerian-Eulerian TFM model is used and the fluid dynamics of the gas-solid fluidized bed incorporated the kinetic theory for solid particles for the bed expansion ratio measurements and pressure drops. Two-fluid models employ the governing equations of conservation of mass and momentum for both phases, the gas and particle as shown in Equations 7 to 10. The TFM allows for the Eulerian–Eulerian description of the fluidized bed, the gas phase (g) and the solids phase (s) being considered for an interpenetrating continuum. Previously, the dynamics of a two-dimensional gas–solid fluidized bed reactor

were studied experimentally and computationally in order to simulate the gas–solid flow and these studies were reported by Taghipour et al [53], Sinclair et al. [54] and Pain et al [55]. Taghipour et al. [53] used a commercial CFD software package, Fluent, and the simulation results compared to those obtained by experiments conducted in a fluidized bed containing spherical glass beads of 250–300μm in diameter. A multifluid Eulerian model incorporating the kinetic theory for solid particles was applied in order to simulate the gas–solid flow. Sinclair et al. [54] tested experimentally interactions between pairs of particles in a gas-solid multiphase vertical pipe. Pain et al. [55] modelled two fluidized beds, one in the bubbling regime and the other in the slugging regime based on TFM simulation with Gidaspow's drag model. Their simulation results showed a stable fluidized bed when the solid volume fraction is close to maximum packing. The Gidaspow's drag model shown in Equations 12 and 13 that is a combination of the Wen and Yu drag model and the Ergun equation has been used for the calculation of the drag coefficient between the gas and solid phases [44]. Solli et al. [56] stated that Gidaspow's drag models fairly captured the bubbling bed behavior while using the Syamlal and O'Brien drag model didn't capture this phenomenon in the TFM simulation.

3.3 Simulation Geometry and Properties

The simulation studies matched the reactor dimensions to previous experimental work conducted in the Andino Research Group [57] that is also reported in the chapter 2 of this dissertation. The simulation was performed on a two-dimensional column reactor with an inner diameter of 7.62 cm and a height of 100 cm. Figure 15a shows the dimensions of the geometry and meshing for the MVA fluidization simulation based on the geometry of the

experimental setup. An example of a solid volume fraction and boundary conditions of the two-fluid method is shown in Figure 15b. Superficial gas velocity from the bottom of the reactor as an inlet condition was generated at 0.02 m/s and the frequency level was fixed at the resonance frequency of 50 Hz, using an amplitude of 1.6 mm. The vibration of the fluidized bed was incorporated in the simulation through the formula of effective gravity that was programmed using Fortran code and interpreted by MFiX 19.2.0 as a user defined function. All parameters used for this simulation are shown in Table 3.

Table 3. Parameters for TFM Simulation

Parameters	Description	Experiment [52]	Simulation
W (m)	Fluidized bed width	0.0762	Same
H (m)	Reactor Height	1	Same
h_0 (m)	Initial packed bed Height	0.11	Same
d_{agg} (μm)	Diameter of agglomerate	-	89.75
ρ_{agg} (kg/m^3)	Agglomerate density	-	130
ρ_g (kg/m^3)	Gas density	1.17 (at 293 K)	Same
μ_g (Pa s)	Gas viscosity	2.12E-05 (at 293 K)	Same
T (K)	Gas temperature	293	Same
U_g (m/s)	Superficial gas velocity	0.02	Same
U_{jet} (m/s)	Microjet velocity	200	Same
D_{jet} (μm)	Microjet diameter	500	Same
f (Hz)	Vibrational frequency	50	Same
A (mm)	Vibrational Amplitude	0.16	Same
ε_0	Initial bed voidage	0.47	Same

The time step of the simulations was set to 10^{-3} seconds , i.e. one order of magnitude lower than the vibration time (0.02 seconds). Furthermore, the Courant Friedrichs Lewy (CFL) safety factor (also known as the Courant number) was considered for the stability of finite difference discretization. The choice of time step size cannot be independent of the mesh size. Thus, it is necessary to change the time step with changes in mesh size in order to maintain the stability of the numerical solution. The courant number should be less than the stability limit in order to avoid chaotic oscillations when the stability threshold is reached [58]. Ansari et al. [59] considered the timestep and superficial gas velocity to maintain low enough CFL condition for the numerical calculation using the two-fluid model. The CFL condition for stability can be expressed mathematically according to Equation 14.

$$CFL = \frac{|u|\Delta t}{\Delta x} \leq 1 \qquad \text{(Equation 14)}$$

where: u= Maximum velocity

Δt= Time step

Δx= Smallest mesh size

For the simulation in this work, the stability of the explicit numerical scheme was ensured by setting the Courant number to 0.13. This number is attained by limiting the time step number of the simulation. The residuals of the numerically solved governing equations remained below 10^{-3} to obtain sufficiently converged results with the total simulated time of more than 80 seconds. The stability of flow rate and the pressure difference together with the residuals have been checked for all simulation steps. The two-dimensional

computational domain was discretized using square cells of 3.6 mm length in a mesh of 5240 cells in total. Thus, the cell size was one order of magnitude higher than the estimated size of the agglomerate diameter in the TFM simulation.

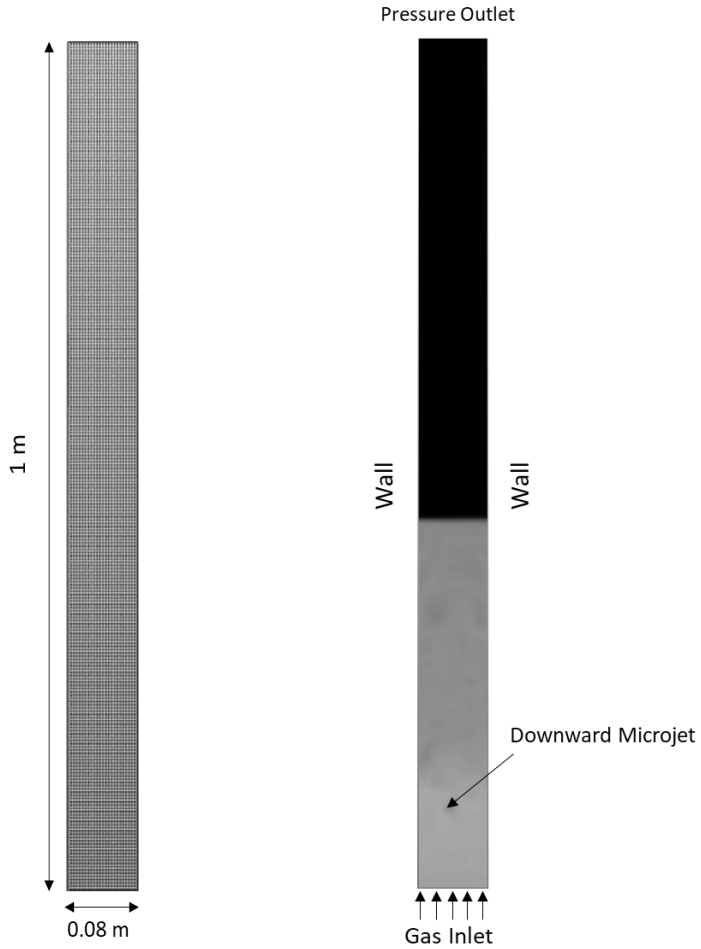

Figure 15. Configuration of Geometry and Boundary Conditions

(a) Domain Dimensions and Computational Meshing (b) Boundary Conditions with Downward Microjet Position

3.4 Validation with Experimental Results

A comparison with previous experimental studies [57] of a microjet and vibration assisted fluidized bed has been performed to examine the applicability of the two-fluid model simulation. Results seem to indicate that TFM models are capable of predicting the realistic dynamic behavior of agglomerates in an MVA fluidized bed under different conditions. However, there are some discrepancies between the two-fluid model simulation results and the experimental measurements with precision errors as shown in Fig. 16. The operating conditions (shown in Table 4) for both experimental work and simulation are identical. The bed height of TFM simulation increased up to 60 seconds and upheld its height until 90 seconds. This behavior is close to an experimental fluidized bed's expansion behavior. The minor difference in fluidization behaviors is due to the limitations in considering the electrostatic forces between the particles and the agglomeration process in a real experiment. These restrictions would require further computational confirmations with additional experimental work and analytical techniques that are currently unavailable at ASU. Table 4. shows the nondimensional height and pressure drop values of experiment and TFM simulation at 80 seconds. The fluidized bed height and pressure drop showed very good agreement between the numerical simulations and experimental results.

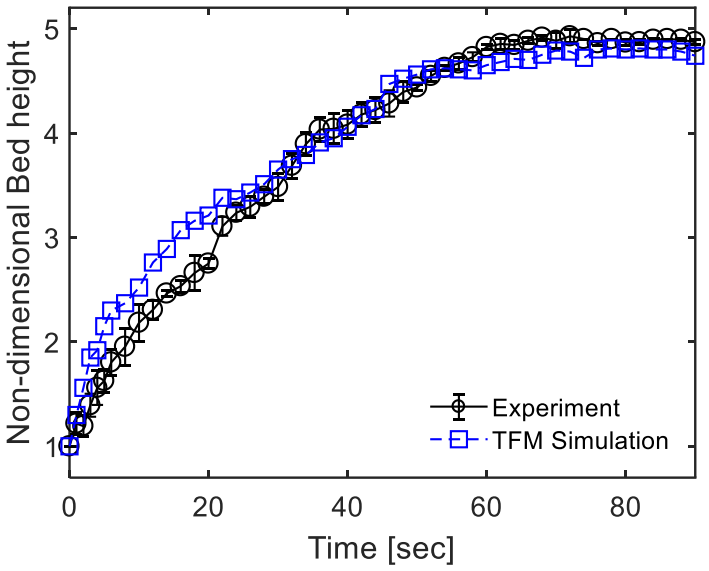

Figure 16. MVA Fluidized Bed Height over Time (Comparison between TFM Simulation and Experiment). Errors in the Data represent Repeatability.
Data Points for this Figure are included in Appendix B, Table B.2.

Table 4. Parameters used for Validation between Experimental Work and TFM Simulation at 80 Seconds

Parameter Simulation	Description	Experiment	TFM
$H_{nondimensional}$ (= H/H_0)	Nondimensional bed height	4.85	4.8
△P	Pressure drop [Pa]	89.63	90

3.5 Gas Velocity Distribution in the MVA Fluidized Bed

The main difference from previous fluidized beds is the gas velocity profile in the bed due to microjet assistance in the MVA system that influences the forces acting on agglomerates. The two-fluid simulation using the opensource software MFiX has been used to obtain the gas-phase velocity profile in the MVA fluidized bed. As we assumed, the gas phase velocity showed one order higher magnitude than superficial gas velocity that participates

in the force balance modelling for agglomerate size estimation. It is expected that we were able to obtain realistic agglomerate size distribution through the overall gas velocity profile in the MVA fluidized bed system. The vertical gas velocity profile is shown in Fig. 17.

3.6 Force Balance in Fluidized Bed

The forces acting on a fluidized agglomerate are divided into two main categories: adhesion and separation forces. Their classification into the two groups varies in previously published papers [60,61]. Van der Waals force is regularly in the adhesion group, while gravity, collisional and drag forces are in the separation group. The gravity-buoyancy force is evaluated with the effective density of the agglomerate. Various equations are proposed to calculate the van der Waals forces between two spherical agglomerates depending

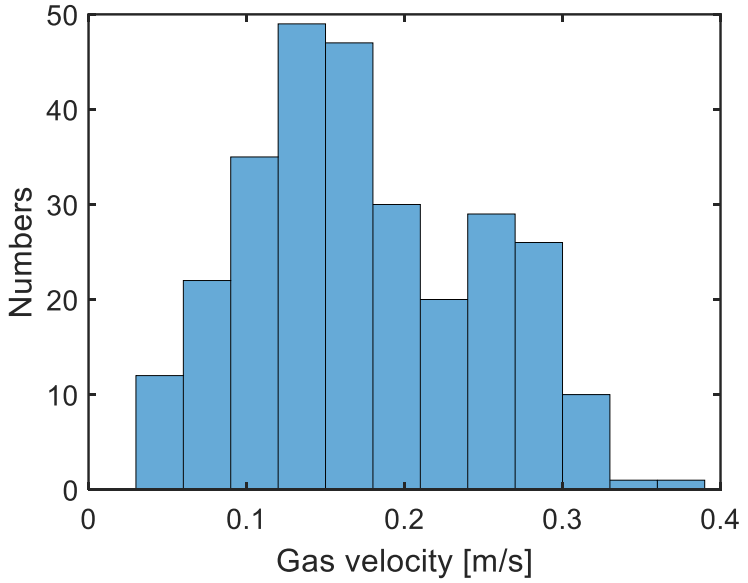

Figure 17. Gas Velocity Distribution in the MVA System under Condition of U_g= 0.03 m/s, f= 50 Hz and A= 0.016 mm. Data Points for this Figure are included in Appendix B, Table B.3.

on the geometrical parameters [60,61]. In a fluidization system, the major forces acting on a fluidized agglomerate are van der Waals and collisional forces rather than gravitational and drag force as shown in Fig. 18. As we can see, the dominant adhesion and separation forces in the fluidized are van der Waals force and collision force, respectively. Therefore, a simple but representative force balance equating the effective forces can give valuable approximations to the agglomerate size in the fluidized bed. To simplify the force balance model analysis, the agglomerates are assumed to be non-porous spheres and the size of the agglomerates is represented by a mean diameter. Additionally, the reactor wall effect and elutriation are not considered, and the effect of electrostatic forces and liquid bridging forces are not considered as well. Fig. 19 compares the two major forces, van der Waals and collisional forces in the fluidized bed as a function of the agglomerate size. Additionally, two dominant forces as a

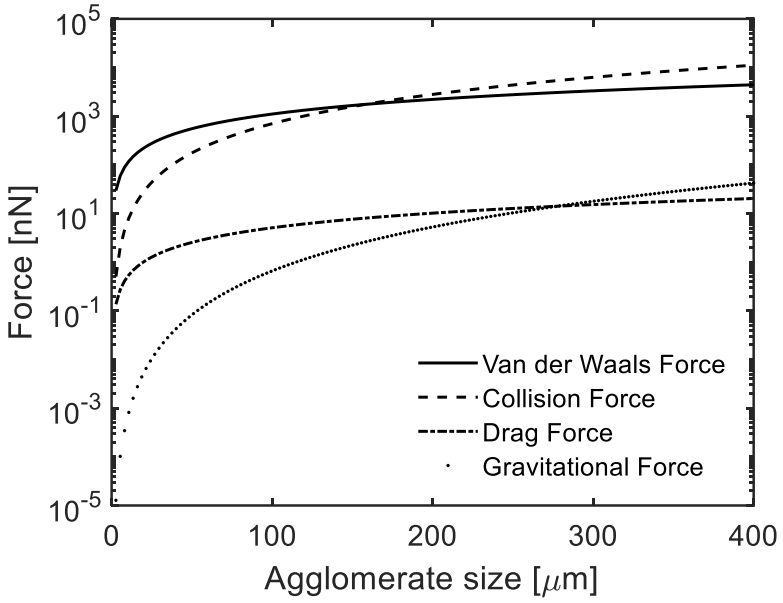

Figure 18. The Forces acting on the Agglomerates in a Fluidized Bed.

function of agglomerate size is shown for one order of magnitude differences in gas velocities acting on the agglomerate, i.e. 0.03 and 0.3 m/s. The value of an agglomerate size based on a force balance model can be derived when the difference between adhesion and separation forces is zero, when the collision and Van der Waals forces have the same magnitude. As shown in Fig. 19, increasing the gas velocity by one order of magnitude amplifies the collisional force in the fluidized bed, assuming constant adhesive Van der Waals force. These changes decrease the agglomerate size.

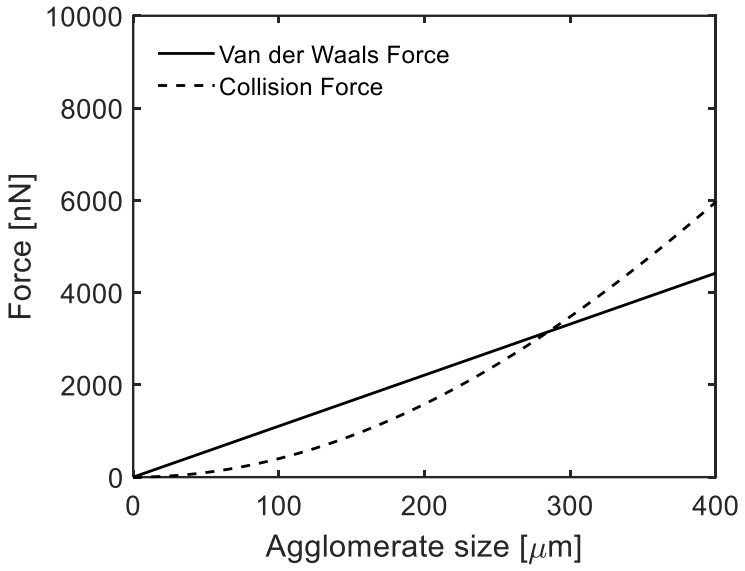

(a)

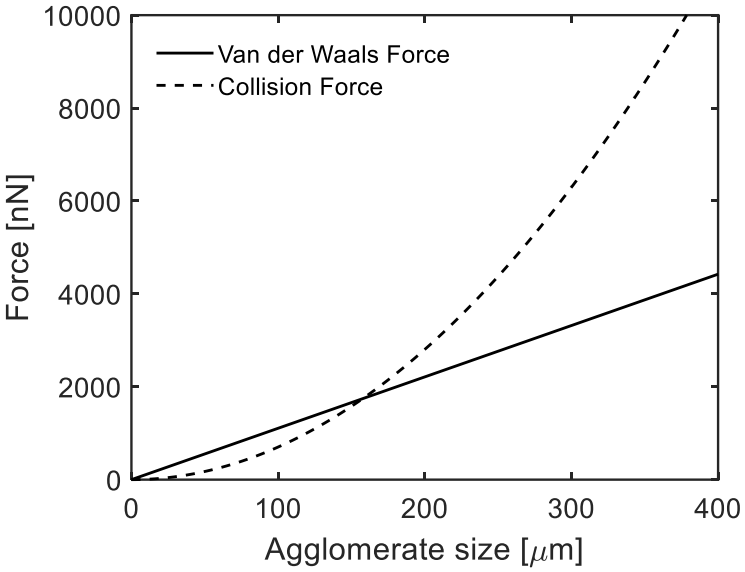

(b)

Figure19. Two Dominating Forces, Van der Waals and Collision Forces versus Agglomerate Size. The Crossing Point between Two Forces is the Predicted Agglomerate Size based on Force Balance Modeling. (a) Gas Velocity at 0.03 m/s, (b) Gas Velocity at 0.3 m/s

3.6.1 Van der Waals Force

Previously, numerous equations were proposed for estimating the van der Waals adhesion force between two solid bodies that were pulled together by adhesion forces when there was a flattening at the location of contact [62]. Krupp et al. [63] stated the van der Waals force can be expressed as attractive forces pulling two solids with flattening location of the contact. There are assumptions of small non-elastic deformation, absence of electrostatic components, and surfaces in the presence of contacting asperities from the surface roughness. Using the assumptions, the contact force can be formulated as:

$$F_{vdw} = \frac{h_w \varphi R_a}{16\pi\delta^2}\left(1 + \frac{h_w \varphi}{8\pi^2\delta^3 H_r}\right) \qquad \text{(Equation 15)}$$

where: h_w = Lifshitz-van der Waals constant ($h_w = \pi H_a 4/3$)

R_a = Agglomerate radius

φ = Solid fraction of the agglomerate

δ = Contact distance between two solids

The van der Waals force is based essentially on the macroscopic theory of Lifshitz that is derived by equations from dispersion theory so that the interaction forces can be calculated directly from the imaginary parts of the complex frequency-dependent dielectric constants of the adherents, which in turn are obtained most simply from reflection measurements [63]. The Lifshitz-van der Waals constant (h_w) depends on the nature of interacting bodies and the surrounding medium. This constant can be calculated from the Hamaker constant (H_a) [64] which is the coefficient estimated by integrating the van der Waals attractive potential over the volume and number of molecules for porous structures. And H_r is

Young's modulus of agglomerate that characterizes the hardness of agglomerate and formulated as [60,61],

$$H_r = 17.1\varphi^4 \left(\frac{E_p^2 \gamma}{d_p}\right)^{\frac{1}{3}} \qquad \text{(Equation 16)}$$

where: E_p = Young's modulus of a single nanoparticle

γ = Interface energy

d_p = primary particle diameter

The Young's modulus of agglomerate, Hr, was estimated by Kendall et al. [65,66] who stated that the experimental data on zirconia, titania, alumina and silica assemblies supported the elasticity theory for assemblies. The Lifshitz van der Waals constant is multiplied by the solid fraction to account for the void fraction of the porous agglomerate when calculating the contribution of the van der Walls forces. This results in the final formula of the van der Waals force between two identical solid porous agglomerates as shown in Equation 15.

3.6.2 Collision Force

In the fluidized bed, agglomerates are constantly colliding with each other and the collision between agglomerates can noticeably decrease their size. Based on the theory of elasticity [67], the collision force depends on the displacement of maximum compression that is a function of the particle density, Young's modulus, Poisson's ratio, particle size and relative collision velocity of the agglomerates. The following expression assumes that identical elastic bodies, agglomerates colliding in a fluidized bed can be represented as [68],

$$F_{coll} = 0.166\left(\frac{\pi V_r^6 \rho_{agg}^3}{k^2}\right)^{1/5} d_{agg}^2 \qquad \text{(Equation 17)}$$

where: V_r = Relative collision velocity

ρ_{agg} = Agglomerate density

d_{agg} = Agglomerate diameter

And the factor k which depends on Young's modulus and the Poisson's ratio of the particle [67].

$$\mathrm{k} = \frac{1 - v^2}{\pi H_r} \qquad \text{(Equation 18)}$$

where: v = Poisson's ratio

H_r = Young's modulus

Zhou and Li et al. [68] assumed that the two agglomerates that are vertically aligned come into an elastic collision. They stated that two identical spherical agglomerates collide with an estimated relative collision velocity. The estimated relative velocity of the agglomerate depends on the behavior of fluidized bed and ABF type powders, it can be expressed by Equation 19.

$$V_r = \left(1.5\bar{P}_{s,n} D_b g \epsilon_b\right)^{0.5} \qquad \text{(Equation 19)}$$

where: $\bar{P}_{s,n}$ = Dimensionless particle pressure

D_b = Bubble diameter

ϵ_b = Void fraction of the fluidized bed

$\bar{P}_{s,n}$ is the dimensionless average particle pressure of a non-sticky system that is developed based on compaction and expansion theoretical approach by Horio and Iwadate et al. [69]. The important parameter of relative velocity equation is bubble diameter, especially for ABF type powders. Darton et al. [70] studied the bubble size in the fluidized bed and their model predicted the bubble growth with reactor height. The model captured the bubble sizes well near the distributor up to 0.6 meters, but the linear growth model over-estimated the bubble size in large, deep fluidized beds. Farshi et al. [71] stated that the equations by Mori et al. [72] and Rowe et al. [73] fitted well for bubble diameter predictions in a bubbling fluidized bed. Two common variables in the previous models for calculating the bubble diameter are the ratio of gas velocity to minimum fluidization velocity and the cross-sectional area of the reactor. Yasui et al. [74] showed that the bubble diameter is proportional to the primary particle diameter although Park et al. [75] showed that the bubble diameter to be proportional to gas flow rate and particle diameter. Kato et al. [76] reported that the bubble diameter is dependent on the particle density. In this work, the bubble diameter in the fluidized bed is calculated by Guo's model [77] since their particle characteristics, reactor size and operating conditions were close to our conditions [57]. The bubble diameter in a fluidized bed defined as Equation 20.

$$D_b = 0.652\left(A_t\left(|u_i| - u_{mf}\right)\right)^{2/5} \qquad \text{(Equation 20)}$$

where: A_t = Cross-sectional area of fluidized bed

u_i= Local gas velocity (i: each cell)

u_{mf} = Minimum fluidization velocity

In the current work, the gas velocity, u_i, considered as local gas velocity for bubbling diameter estimation instead of using a single representative superficial gas velocity [7,61,68,78]. This is due to the maximum gas phase velocity from the TFM simulation was one order higher than superficial gas velocity due to microjet assistance in the MVA system. By considering the local gas velocity, we are able to obtain an explicit agglomerate size distribution in the MVA system in place of singular representative agglomerate size. The minimum fluidization velocity of agglomerates was empirically estimated by Leva et al. [79]. In this work, we already experimentally obtained the minimum fluidization velocity, 0.009 m/s for the MVA system. All parameters used for calculation of the force balance model are shown in Table 5.

Table 5. Parameters used for Calculation of the Forces acting on TiO_2 P25 Agglomerates

Parameter	Description	Values
d_p	Primary particle size [nm]	21
ρ_p	Primary particle density [kg/m^3]	4000
d_{agg}	Agglomerate particle size [μm]	90
ρ_{agg}	Agglomerate density [kg/m^3]	130
φ	Agglomerate solid fraction	0.03
ε	Fluidized bed solid fraction	0.1
H_a	Hamaker constant	1.38E-19
δ	Distance between agglomerates [m]	4E-10
E_p	Nanoparticle's Young's modulus [Pa]	2.34E+11
Γ	Work of adhesion [J/m^2]	0.8
k	Poisson's ratio and Young's modulus of agglomerate [Pa^{-1}]	3E-6
$\bar{P}_{s,n}$	Dimensionless average particle pressure	0.077
μ	Fluid viscosity [N-s/m^2]	0.000018
ρ_f	Fluid density [kg/m^3]	1.25
A_t	Cross-sectional area of the reactor [m^2]	0.00456
g	Gravitational acceleration [m/s^2]	9.81

3.7 Agglomerate Size Distribution in the MVA System

The force balance model based on the adhesion and separation forces was developed to estimate the size distribution in the MVA fluidized bed. There are complexities of fluidized agglomerates, the force balance model includes some assumptions. Two dominating forces, collision and van der Waals forces acting on agglomerates are considered and the agglomerates are assumed to be spherically shaped with same sizes. For the force balance

model, the collision forces are assumed to only vertical 180 degrees angle between two identical particles. These assumptions showed a reasonable impact on the accuracy of the force balance modelling prediction that has a strong dependence on the agglomerate's density and solid fraction [80]. Thus, the vertical gas velocity profile from the two-fluid model simulation has been used to evaluate the overall agglomerate distribution in the MVA fluidized reactor. The agglomerate size can be obtained by equating the major adhesion Equation 15 and major separation force Equation 17. The agglomerate sizes depend on operating conditions and constant parameters of material properties. For example, the increment of Hamaker coefficient will increase the agglomerate size and increasing Young's modulus or solid fraction will decrease the agglomerate size. The force balance model showed that excess velocity at different locations has a major effect on the agglomerate size since the maximum vertical gas velocity is one order higher than superficial gas velocity due to the microjet assistance. Fig. 20 shows the agglomerate size distribution over the MVA fluidized bed calculated by force balance model. The range of agglomerate sizes in the MVA fluidized bed is 40 to 100 microns with average size, 67.12 microns from the

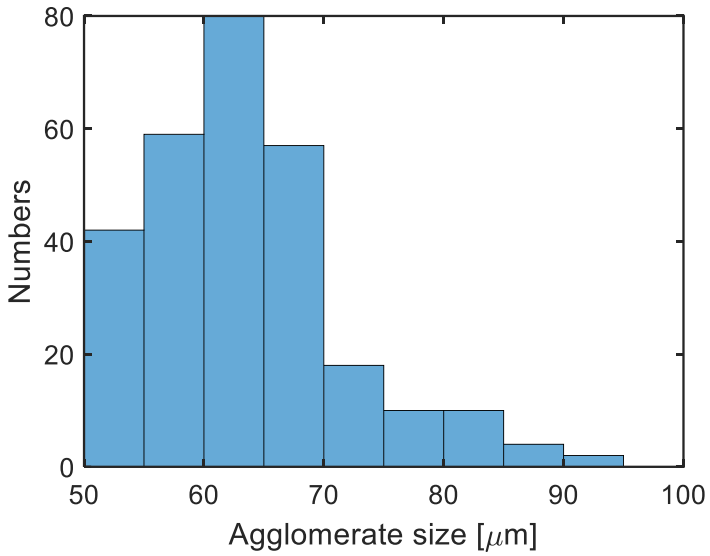

Figure 20. Agglomerate Size Distribution in the MVA System based on the Simulation Work Data Points for this Figure are included in Appendix B, Table B.4.

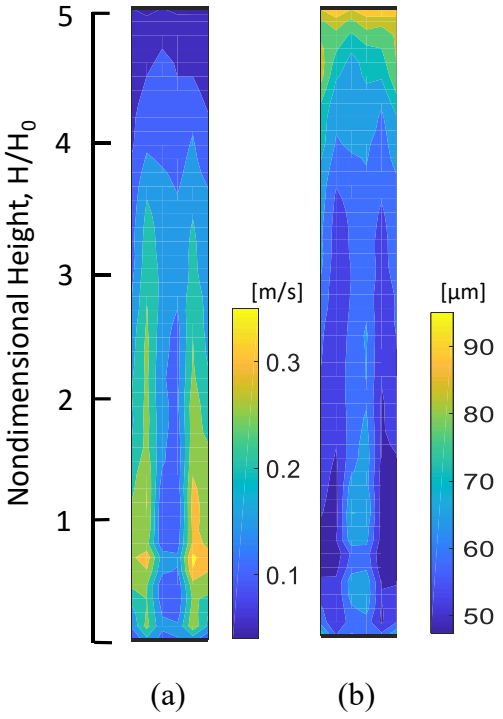

Figure 21. 2-Dimensional Results of (a) Gas Velocity (m/s) and (b) Agglomerate Size (µm) Profile up to Nondimensional Height, H/H_0=5.

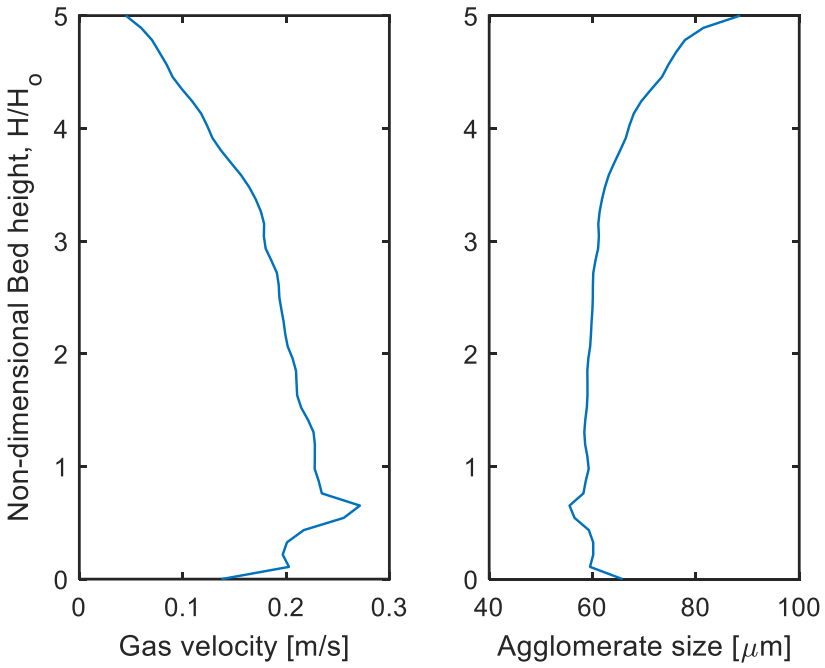

Figure 22. Averaged Values of (a) Gas Velocity and (b) Agglomerate Size at each Horizontal (Radial) Distance up to Nondimensional Height, H/H_0=5. Data Points for this Figure are included in Appendix B, Table B.6.

force balance model. The agglomerate size distribution where the large gas velocities near microjet generated small agglomerate sizes less than 50 microns and near the top of the fluidized bed where low gas velocities generated comparably large agglomerates more than 70 microns. 2-Dimensional gas velocity and corresponding agglomerate size distribution are shown in Fig.21. The results are 80 to 90 seconds averaged (10 seconds) gas velocity and agglomerate size profile in the MVA system. The gas velocity profile shows that microjet flow bounced at the bottom and escaped upward near the wall. The agglomerate sizes are calculated by the force balance model (Equation 15 & 17), and most of the larger agglomerates are located at the top of the fluidized bed. Fig. 22 shows the distribution of

gas velocity and agglomerate size up to nondimensional height, 5. The gas velocity profile obtained from the result of the TFM simulation at 80 seconds and each velocity values were used for the calculation of agglomerate sizes from force balance model.

3.8 Experimental Results of the Agglomerate Size and Model Validation

An ex-situ sampling method was used to analyze the agglomerates size distribution in order to attempt to validate the force balance model. In the previous chapter, the model based on the force balance was developed to estimate the agglomerate size distribution in the MVA fluidized bed. For the experimental method, double-sided carbon tape attached to a SEM (Scanning Electron Microscope) stub that was directly exposed to the top of the initial static bed and fluidized bed using a sampling rod that was connected to the SEM stub. As shown in Figs. 23 and 24, the carbon tape samples of initial static bed TiO_2 P25 showed a larger amount of complex agglomerates between the sizes of 44 to 288 μm as compared to the sizes of the fluidized bed's agglomerates, 33 to 183 μm, and these agglomerates were highly porous and chain-like clusters formed by aggregates with rough surfaces. The opensource software ImageJ was used to analyze the particle size distribution from SEM images. Fig. 25 shows the whisker plot of initial static bed and fluidized bed of TiO_2 P25 agglomerates from SEM results.

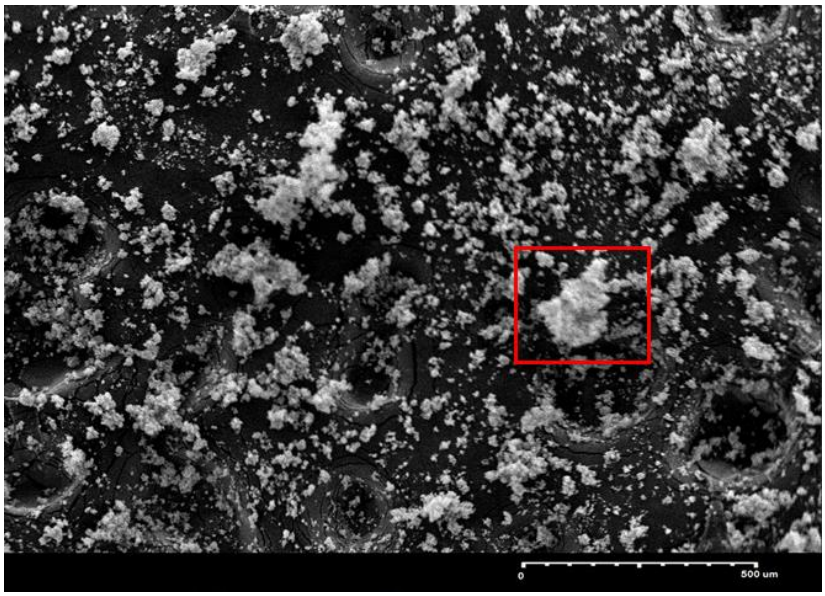

(a)

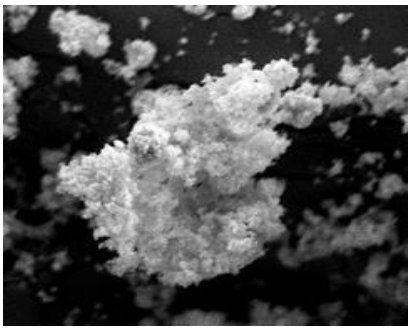

(b)

Figure 23. SEM Image of TiO_2 P25 at the Top of the Initial Static Bed. The SEM Picture gathered from Ex-situ sampled Agglomerates on the Carbon Tape. (a) SEM Image of Agglomerates at 98 Times Magnification. Micron Marker Scale: 500 μm (b) Closed up View of Agglomerate in the Red Square Box.

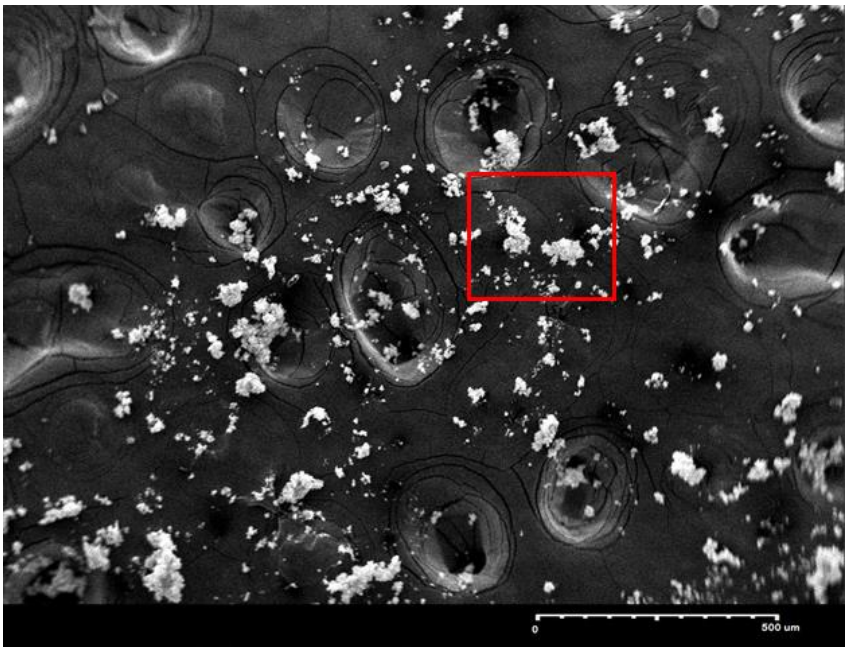

(a)

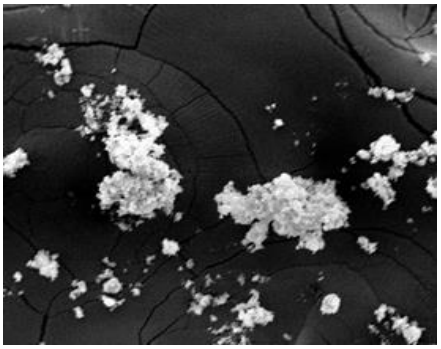

(b)

Figure 24. SEM Image of TiO_2 P25 at the Top of the MVA Fluidized Bed. The SEM Picture gathered from Ex-situ Sampled Agglomerates on the Carbon Tape. (a) SEM Image of Agglomerates at 98 Times Magnification. Micron Marker Scale: 500 μm (b) Closed up View of Agglomerate in the Red Square Box.

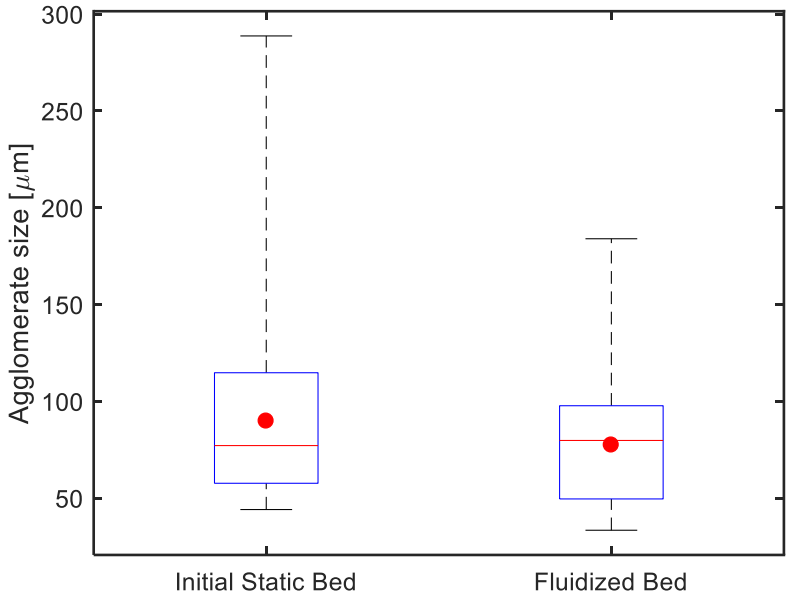

Figure 25. Whisker Plot of Initial Static Bed and Fluidized Bed from SEM Image. The Blue Box encompasses the Second and Third Quartiles and the Red Lines are the Median Values, divided by a Red Line corresponding to the Median and the Red Circles are the Mean Values.

The averaged agglomerate sizes of initial static bed and fluidized bed are 89.7 µm and 77.3 µm, respectively. The mean size of fluidized bed agglomerates decreased compare to the initial static bed condition due to vibration and microjet assistance. All samples were characterized by SEM imaging at Eyring Materials Center at Arizona State University. The imaging device, SNE-4500M Tabletop, was used to evaluate the general size distribution and morphology of rough surfaces. From the force balance model, the mean size at the top of the fluidized bed was 88.56 µm that is % overly estimated compared to 77.3 µm of the experimental result. This is mainly owing to the force balance model assumptions to

estimate the complex properties of agglomerates and nanoparticle clusters. In this work, the force balance model development is simplified by neglecting the fractal morphology of the agglomerate and assuming the agglomerates to be perfect elastic spheres with a smooth surface.

4. APPLICATION OF THE MICROJET AND VIBRATION ASSISTED FLUIDIZATION SYSTEM IN CO_2 CAPTURE

4.1 Introduction

Carbon capture and storage (CCS) is a promising option for CO_2 reduction. Numerous methods to capture carbon dioxide have been proposed, including post-combustion carbon capture processes focusing on advanced solid adsorbents and fluidization/membrane systems. The use of a fluidized bed reactor is one of the promising techniques for CO_2 capture in a post-combustion process. The main benefits of fluidization are high gas–solids contact efficiency and the continuous regeneration of adsorbents. Li et al. [81] studied CO_2 adsorption capacity over dry $K_2CO_3/MgO/Al_2O_3$ adsorbents of 1 to 1.8 mm sizes in a fluidized bed reactor. The result showed that the total CO_2 adsorption capacity of the new sorbent reached 109.6 mg of CO_2/g of sorbent in the bubbling regime at 60 ℃. Li and Lu et al. [82,83] utilized enhanced calcium-based adsorbents such as CaO-$MgAl_2O_4$, $CaCO_3$–CaO and CaAc2–CaO. The calcium oxide containing materials have high reactivity, capacity toward CO_2 and low material cost. Li [82] stated that a long-term stable CO_2 absorbent not only requires the size of starting CaO absorbents to be small but also requires these small CaO particles to be able to remain highly dispersed after multiple carbonation-decarbonation cycles. Valverde et al. [84] mixed silica nanopowders with calcium hydroxide powder to enhance the CO_2 adsorption efficiency in a fluidized bed. In this way, the contact efficiency between the CO_2 adsorbent and CO_2 in the fluidized bed is greatly

enhanced. Experimental results show that the improvement of $Ca(OH)_2$ fluidizability serves to enhance the carbonation reaction in the fluidized bed.

From previous research, there was an attempt to enhance the CO_2 adsorption capacity with various solid sorbents in a fluidized-bed reactor [85-91]. Vincenzo et al. [92] investigated the performances of a photoreactor with different photocatalyst formulations, including Cu/TiO_2, Ru/TiO_2 and Pd/TiO_2. Veneman et al. [93] applied an integrated approach, both sorbent and process development, to develop a highly efficient CO_2 capture process. Sorbent testing using thermal gravimetric analysis (TGA) was combined with lab scale testing in a circulating fluidized bed reactor (CFB) with sorbent regeneration in a CO_2 atmosphere to produce a high purity CO_2 product stream.

In this dissertation, CO_2 capture efficiency and bed breakthrough time were examined in the MVA fluidized bed system using titanium dioxide (TiO_2) as the adsorbent. Operation of the system in the full microjet and vibration assisted (MVA) mode was compared to operation employing just the vibration assistance (in vibrating fluidized bed or VFB mode). In addition, the sustainability of the system was explored in order to suggest future areas for improvement.

4.2 Experimental System and Conditions

The overall schematic of the CO_2 capture experimental setup is shown in Fig. 26. The CO_2 adsorption experiments were performed using a 1% CO_2, 99% nitrogen gas mixture at atmospheric pressure and ambient temperature. Pure nitrogen gas was used as the diluent in the fluidized bed system using the optimized operating conditions for the MVA with TiO_2 nanoparticles (described previously). The fluidized bed system was operated either

with just the vibration and gas flow (vibrating fluidized bed or VFB mode) or with both the microjet and vibration assistance (MVA mode) and gas flow. Secondly, the gas mixture, 1% CO_2 in nitrogen was subsequently passed through the fluidized bed from the bottom of the reactor using a three-way valve. The outflowing gas was delivered to a CO_2 analyzer (Bacharach Model 2835) to measure the CO_2 concentration as a function of time. The CO_2 concentration data points were obtained every 5 seconds for a total of 2 minutes. Additionally, we tested the CO_2 capture capacity in the MVA system using same sorbents with 8 cycles without a regeneration process, in order to examine the bed's adsorption capacity over time.

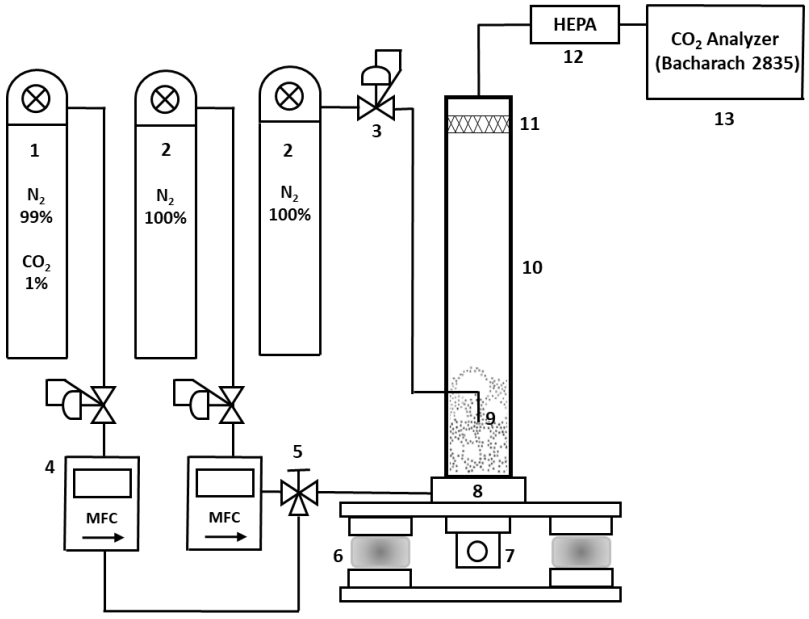

Figure 26. Schematic of the CO_2 Capture Fluidized Bed System. Key: 1: Compressed Gas Cylinder (N_2 99% + CO_2 1%), 2: Compressed Gas Cylinder (N_2 100%), 3: Pressure Regulator, 4: Mass Flow Controller, 5: Three-Way Valve, 6: Vibration Isolator, 7: Magnetic Vibrator, 8: Gas Distributor 9: Downward Micronozzle, 10: Fluidization Reactor, 11: Pre-Filter, 12: HEPA Filter, 13: CO_2 Analyzer

4.3 CO_2 Breakthrough Time and Capture Capacity

In this work, the CO_2 breakthrough method was used to measure the adsorption equilibrium capacity of 1% carbon dioxide with nitrogen as the carrier gas. We considered the breakthrough time as the point in time when 10 ppm of carbon dioxide concentration was detected. The kinetic adsorption capacity at the breakthrough point can be determined by the mass balance of carbon dioxide. Based on the mass balance of CO_2, the total and breakthrough capacities of CO_2 gas could be determined using equations 21 and 22,

$$q = \frac{Q t_s C_{in}}{22.4W} \qquad \text{(Equation 21)}$$

$$t_s = \int_0^t \left(1 - \frac{C_{out}}{C_{in}}\right) dt \qquad \text{(Equation 22)}$$

where: t_s = Mean residence time (min)

C_{out} = Outlet concentration of CO_2

C_{in} = Inlet concentration of CO_2

q = Equilibrium adsorption capacity of CO_2 (mmol/g)

t = Adsorption time (min)

Q = Volumetric flow rate (mL/min)

W = Mass of the sorbent (g)

The equilibrium adsorption capacity, q, was measured by utilizing the concept of mean residence time derived by the C_{out}/C_{in} curves as a function of adsorption time. The outlet CO_2 concentrations were measured at 293 K and 1 atm conditions. Then, the CO_2 concentrations were converted to standard conditions of 1 atm and 273 K by using the ideal gas law.

4.4 Results

Fig. 27 illustrates the MVA and VFB fluidized bed's C_{out}/C_{in} curves as a function of time in minutes. The MVA system showed to lengthen the breakthrough time, 0.5 minutes, compared to VFB's breakthrough time, 0.3 minutes. Also, the MVA system's total adsorption time was 1.7 minutes, which is longer than the 1.4 minutes of the VFB system. Fig. 28 shows the comparison between the MVA and VFB systems' equilibrium adsorption capacity by Equation 21. The MVA system adsorbed 0.083 mmol/g of carbon dioxide, a value that is 1.2 times higher than the amount of carbon dioxide adsorbed in the VFB system. This result describes the advantage of the MVA system's larger fluidized bed as compared to the VFB system in terms of CO_2 capture.

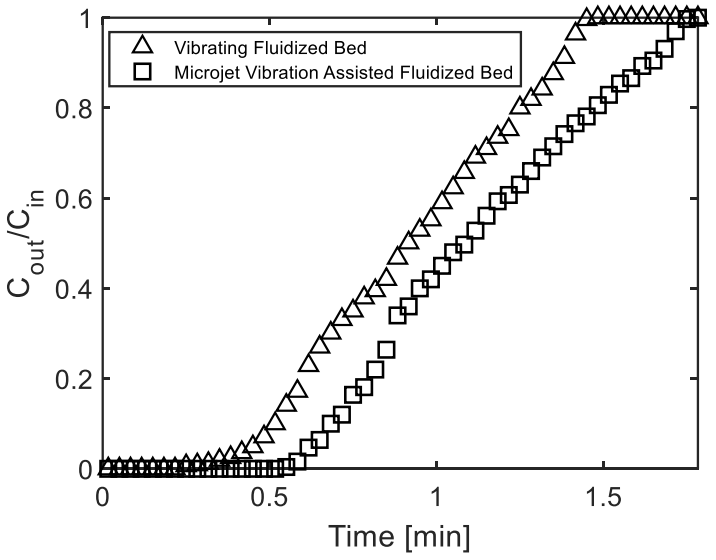

Figure 27. Breakthrough Curves of CO_2 on TiO_2 Sorbent in VFB and MVA Fluidization Systems. Flow Rate, 0.02 m/s; Feed Gas, 1 vol% CO_2; 99 vol% Balance Gas of N_2; Amount of TiO_2 Sorbent, 50 g. Data points for this Figure are included in Appendix C, Table C.1.

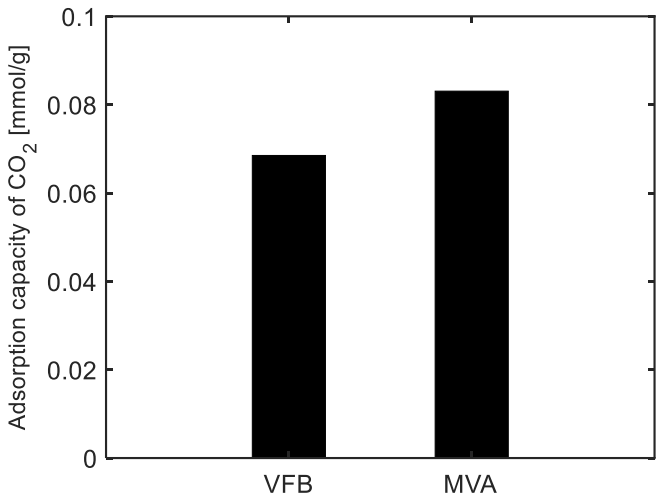

Figure 28. Total Capacities of CO_2 over the TiO_2 Sorbent for Multiple Adsorption Cycles in the MVA Fluidized Bed. Flow Rate, 0.02 m/s; Feed Gas, 1 vol% CO_2; 99 vol% Balance Gas of N_2; Amount of TiO_2 Sorbent, 50 g.

The adsorption capacity gradually decreased with every cycle and the adsorption capacity decreased by 30.3% after the 8th cycle as compared to the initial stage, as shown in Fig. 29. Fig. 30 gives the outflow concentration curves of CO_2 against the adsorption time at 1st and 8th cycle test. It took approximately 1.2 minutes to saturate the sorbent during the 8th cycle. The CO_2 concentration slowly increased to its feed concentration and did not change anymore after 0.3 minutes when the adsorption process reached equilibrium. For the practical test, the MVA system not only possesses high capture capacity but also showed stable performance for multiple adsorption cycles. As shown in Fig. 29, the CO_2 adsorption capacity of the MVA system gradually changed up to 8 cycles, indicating that the adsorbent needed regeneration after multiple cycles of adsorption in the MVA fluidized bed. While this result might have an interest for industrial applications involving the use of fluidized bed adsorbers, there are still a number of limitations to be addressed in future

work.

A different adsorbent would be useful in MVA fluidized bed applications involving low superficial velocities, in order to avoid particle elutriation and large bubbling at high gas velocities. Moreover, when vibration assistance is used, which requires additional energy consumption for continuous operation, the use of renewable sources or waste vibrational energy in the multiple adsorption and desorption cycles would enhance the sustainability of the process.

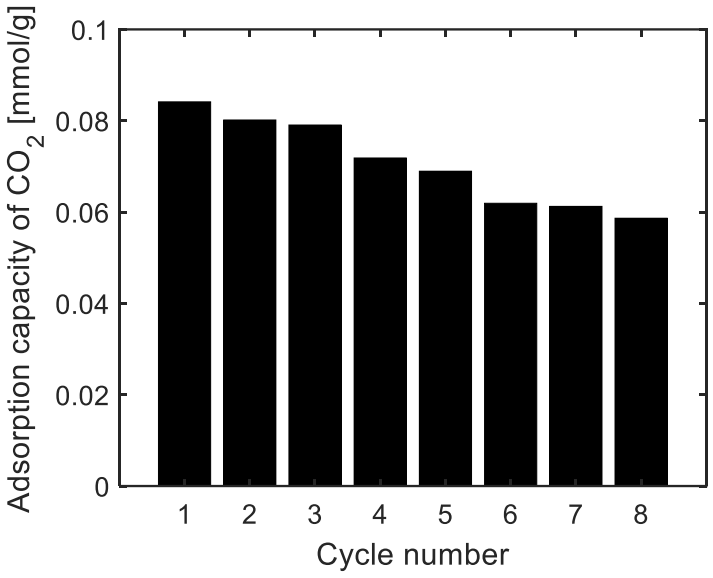

Figure 29. Total Capacities of CO_2 over the TiO_2 Sorbent for Multiple Adsorption Cycles in the MVA Fluidized Bed. Flow Rate, 0.02 m/s; Feed Gas, 1 vol% CO_2; 99 vol% Balance Gas of N_2; Amount of TiO_2 Sorbent, 50 g. Data Points for this Figure are included in Appendix C, Table C.2.

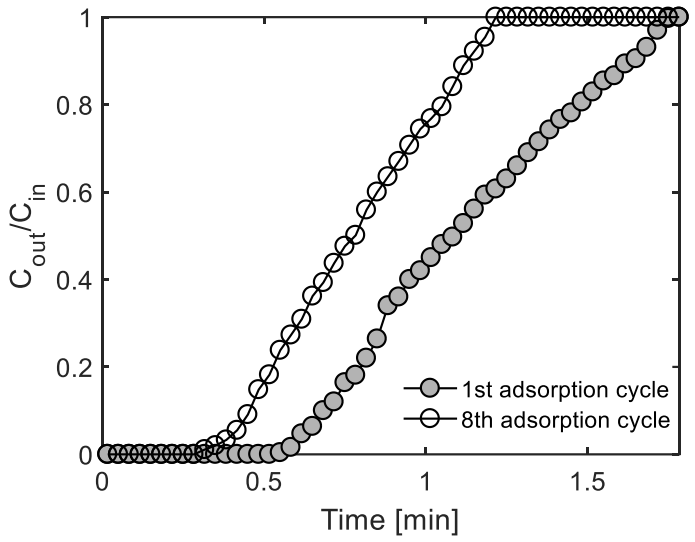

Figure 30. Breakthrough Curves of CO_2 over the TiO_2 Sorbent for 1st and 8th Adsorption Cycles in the MVA Fluidized Bed. Flow Rate, 0.02 m/s; Feed Gas, 1 vol% CO_2; 99 vol% Balance Gas of N_2; Amount of TiO_2 Sorbent, 50 g. Data Points for this Figure are included in Appendix C, Table C.3.

4.5 Sustainability Considerations

Additional work was undertaken to analyze the sustainability of the proposed system. Generally, solvent-based post-combustion system requires large input energy from current power plants because of its high energy penalty in the solvent regeneration process and the environmental impacts of solvent degradation. Our proposed MVA fluidized bed indirectly emits CO_2 gas because of the energy that is required to operate the magnetic vibrator, flow controller, and CO_2 sensor. Thus, finding ways to lessen the MVA system's required carbon footprint for operating is very important. Therefore, we compared the amount of CO_2 captured by the MVA system and the amount of CO_2 that would be emitted by operating the MVA system if energy for the MVA was generated by using different fuel types. As we know, different fuels emit different amounts of carbon dioxide concerning

the energy they produce when burned. For example, the carbon intensity from the coal power plant is 0.328 kgCO2/kWh based on EIA (U.S. Energy Information Administration). The main energy required for the MVA system during the first adsorption cycle was 0.0048 kWh, primarily from the magnetic vibrator. By simple calculation (see Appendix C), we know that 0.00157 kgCO_2 is emitted when the energy input for the MVA system delivered from a coal power plant. This CO_2 emission amount from the operation of the MVA is one order of magnitude higher than the 0.000116 kg of CO_2 that would be captured by MVA system during the first sorption cycle as shown in Fig. 28 While this imbalance in the CO_2 emissions is not desirable, it does provide additional opportunities for design changes. For example, if a different fuel is used to generate energy for the MVA system, the amount of carbon dioxide that is released from the operation of the MVA could be reduced by a significant amount. Table 6 provides information on the carbon intensities of different fuel types. Furthermore, Fig. 31 presents the CO_2 emissions that would result from the use of different fuel types in the MVA operated with TiO_2 versus other hypothetical adsorbents that would have higher CO_2 adsorption capacities as compared to TiO_2. Fig 31. provides an initial design criterion for the sorbent that could be used in an MVA system that is employed for CO_2 capture, assuming that the sorbent maintained its adsorption capacity over time. Of course, the regeneration process would have to be considered However, the regeneration process would be specific to the adsorbent that would be chosen. Renewable energy sources such as solar or wind energy could also be considered as energy sources for the MVA, depending on the location and weather conditions. Furthermore, wasted vibrational energy could also be considered since there are vibrational energy sources from

a gas turbine, generator and motors in power plants. Recently, research groups developed the novel sorbents to enhance mass-transfer performance for CO_2 capture. Park et al. [94] developed a nanoparticle organic hybrid materials (NOHMs). NOHMs enhanced mass transfer in CO_2 capture because of the unique pathway network that is created in them for CO_2 to reach specific functional groups. NOHMs promise an effect of combined CO_2 capture and conversion and can be used especially as for CO_2 electro-reduction. However, there are still some challenges for the application of these materials in real life, such as poor stability and high viscosity. Hornbostel et al. [95] developed a micro-encapsulated sorbent (MECS) consist of a CO_2 absorbing material inside a polymer capsule shell. MECS are a promising material for post-combustion carbon capture because of their slow-reacting solvent characteristic and low energy penalty as compared to traditional amine solvents. Therefore, efficient and novel CO_2 capture processes using these sorbents need to be urgently developed and studied.

Table 6. Carbon Dioxide Emissions Coefficients by Fuel (Data from U.S. Energy Information Administration)

Factors	Carbon Intensity [kg $CO_2/10^6$ Btu]
Propane	63.07
Butane	64.95
Diesel Fuel	73.16
Kerosene	72.3
Coal (All types)	95.35
Natural Gas	53.07
Gasoline	71.3
Residual Heating Fuel	78.79
Geothermal	7.71
Municipal Solid Waste	41.69
Tire-derived fuel	85.97
Waste oil	95.25

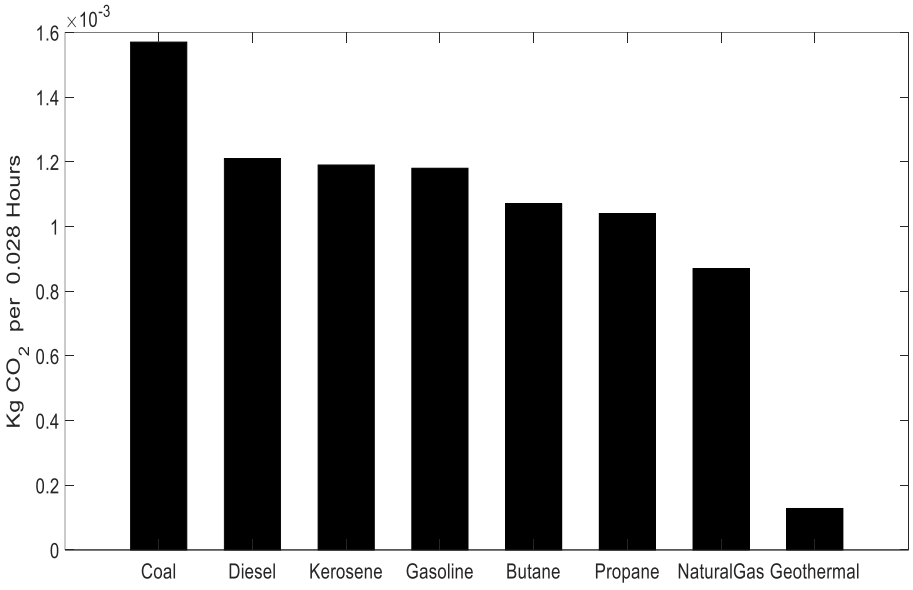

Figure 31. Carbon Dioxide emitted (kg CO_2 per 0.028 hours) by using Different Fuels (e.g. Coal to Geothermal) to create Energy to operate the MVA System

5. CONCLUSIONS AND RECOMMENDATIONS

The fluid dynamic characteristics and fluidization quality of microjet and vibration assisted (MVA) fluidization at varying vibrational intensities and frequencies were investigated. Compared to simple microjet assisted fluidization or a simple vibrating fluidized bed (VFB) system, combined MVA fluidization required a relatively low minimum fluidization gas velocity while maintaining a high nondimensional bed height. By using the combined MVA fluidization technique, smooth fluidization of the nanosized powders and conversion of solid-like flow to fluid-like motion was achieved, even in the

absence of added chemicals (e.g. an alcohol solution) to minimize particle agglomeration. TiO_2 P25 and TiO_2 P90 nanopowder bed height in the MVA system expanded several times more than in the VFB system and showed smooth fluidization without alcohol support, even at high superficial gas velocities. All experiments were repeated multiple times for each powder to ensure the reproducibility of the results. In this work, the optimum operating conditions of vibration (vibrational intensity: 1.6, frequency: 50 Hz) and gas velocity range (0.02 ~ 0.03 m/s) were suggested for the MVA system.

Additionally, the agglomerate size distribution of the MVA system was modeled by balancing the forces on the particles and through ex-situ sampling experiments. The MVA system's gas velocity profile that was obtained by using the MFiX two-fluid simulation showed one order higher velocity as compared to the superficial gas velocity because of the added flow through the microjet. The agglomerate size decreased with increasing gas velocity, as shown by the force balance model coupled with local gas velocity in the MVA system. A mathematical model to predict the agglomerate size distribution was developed based on balancing the van der Waals and collisional forces in the MVA fluidized bed. In addition, the agglomerate size at the top of the MVA fluidized bed was validated with an estimated agglomerate size by using a force balance model, and they were found to be in good agreement.

This work showed that the agglomerates of titanium dioxide nanoparticles served to enhance CO_2 adsorption in a fluidized bed. By adding downward microjet assistance to the vibrating fluidized bed, the effective contact surface and contact time of the adsorbent and CO_2 are increased, thereby increasing the CO_2 breakthrough time and adsorption capacity

during fluidization. These results might have an important role for industrial applications including the use of fluidized bed systems such as adsorption cycle for CO_2 separation technologies. Even though the fluidization experiments were studied without a regeneration cycle, it is expected that the MVA fluidization method would be efficient as compared to previously developed fluidized bed systems in terms of CO_2 adsorption.

The MVA approach should enable the expanded use of nanoparticle fluidization when considering environmental remediation or chemical reaction engineering work where the addition of chemicals is not desirable. These results might have an interest for industrial applications involving the use of fluidized bed reactors, there are still a number of uncertainties to be addressed in future work. Moreover, when sorbents are used, that require the capital cost and energy consumption for regeneration and preparation. Thus, a techno-economic analysis of CO_2 capture using MVA system based on cutting-edge sorbents (e.g. NOHMS [94], MECS [95]) should be carried out in near future.

REFERENCES

1. Granite E. J., & Obrien, T. (2005). Review of novel methods for carbon dioxide separation from flue and fuel gases. Fuel Process Technology, 86, 1423–1434.

2. Seville, J. P. K., Willett, C. D., Knight, P. C. (2000). Interparticle forces in fluidisation: a review. Powder Technology, 113, 261-268.

3. Quevedo, J. A., & Pfeffer, R. (2010). In Situ Measurements of Gas Fluidized Nanoagglomerates. Industrial & Engineering Chemistry Research, 49, 5263-5269.

4. Barletta, D., Donsi, G., Ferrari, G., Poletto, M., Russo, P. (2008). The effect of mechanical vibration on gas fluidization of a fine aeratable powder. Cemical Engineering Research & Design, 86, 359-369.

5. Valverde, J. M., & Castellanos, A. (2006) Effect of vibration on agglomerate particulate fluidization. Aiche Journal, 52, 1705-1714.

6. Zhou, E., Zhang, Y., Zhao, Y., Luo, Z., He, J., Duan, C. (2018). Characteristic gas velocity and fluidization quality evaluation of vibrated dense medium fluidized bed for fine coal separation. Advanced Powder Technology, 29, 985-995.

7. Tahmasebpoor, M., Abadi, R., Noupoor, Y., Badamchizadeh, P. (2016). Model Based on Electrostatic Repulsion and Hydrogen Bond Forces To Estimate the Size of Nanoparticle Agglomerates in Fluidization. Ind. Eng. Chem. Res, 55, 12939-12948.

8. Amjadi, O., & Tahmasebpoor, M. (2018). Improving fluidization behavior of cohesive $Ca(OH)_2$ adsorbent using hydrophilic silica nanoparticles: Parametric investigation. Particuology, 40, 52-61.

9. Fotovat, F., Bi, X. T., Grace, J. R. (2017) Electrostatics in gas-solid fluidized beds: A review. Chemical Engineering Science, 173, 303-334.

10. Pfeffer, R., & Quevedo Jose, A. (2011) Systems And Methods For Reducing Electrostatic Charge In A Fluidized Bed. (2011). United States Patent No. US 7905443 B2.

11. Kuipers J. A. M., Van Duin K. J., Van Beckum F. P. H., Van Swaajj W. P. M. (1993). Computer simulation of the hydrodynamics of a two-dimensional gas-fluidized bed. Comput Chem Eng, 17, 839-858.

12. Pain C. C., Mansoorzadeh S., Gomes J. L. M., Oliveira G. R. E. (2002). A numerical investigation of bubbling fluidized bed dynamics in 2-D geometries. Powder Technology, 128, 56-77.

13. Souza M. P. (2009). Numerical effects on the simulation of gas–solid flow in bubbling fluidized bed using the kinetic theory of granular flow. Dissertação de Mestrado, Faculdade de Engenharia da Universidade Estadual Paulista Júlio de Mesquita Filho, UNESP, Sao Paulo.

14. Huilin L., Yurong H., Gidapow D. (2003). Hydrodynamic modeling of binary mixture in a gas bubbling fluidized bed using the kinetic theory of granular flow. Chem Eng Sci, 58, 1197-1205.

15. Goldschmidt M. J. V. , Kuipers J. A. M. , Van Swaaij W. P. M. (2000). Hydrodynamic modeling of dense gas fluidized beds using the kinetic theory of granular flow: effect of coefficient of restitution on bed dynamics. Sixteenth international

symposium on chemical reaction engineering, 16, ISCRE.

16. An, K., & Andino, J. M. Microjet and Vibration Assisted Fluidization of Nanoparticles. US Patent and Trademark Office Provisional Patent application #62/815,653 filed on 8 March 2019, Invention disclosure #D19-073/M19-140P, Filed with Skysong Innovations at Arizona State University on 12 December 2018.

17. Rollins, S.F. ; J. Smuts, J.; Li, Y.; Andino, J.M. (2016). A GC-VUV Study of the Effects of NO on Carbon Dioxide Photoreduction, Conference Proceedings of the International Conference on Environmental Catalysis, Newcastle, New South Wales, Australia.

18. Zhao, H. L., Liu,L.J., Andino, J. M., Li, Y. Bicrystalline. (2013). TiO_2 with Controllable Anatase/Brookite Phase Content for Enhanced CO_2 Photoreduction to Fuels, J. Materials Chemistry A., 1, 8209-8216.

19. Liu,L.J., Zhao,H.L., Andino,J.M., Li,Y. (2012). Photocatalytic CO_2 reduction with H_2O on TiO_2 nanocrystals: Comparison of anatase, rutile, and brookite polymorphs and exploration of surface chemistry, ACS Catalysis, 2, 1817-1828.

20. Rodriguez, M.M., Peng,X., Liu,L., Li,Y., Andino,J.M. (2012). A Density Functional Theory and Experimental Study of CO_2 Interaction with Brookite TiO_2, J. Phys. Chem. A., 116(37), 19755-19764.

21. Zhang, Q., Gao, T., Andino, J. M., Li, Y. (2012). Copper and Iodine Co-modified TiO_2 Nanoparticles for Improved Activity of CO_2 Photoreduction With Water Vapor, Appl. Cat. B: Env., 257-264.

22. Berkson, Z., Li, Y. and Andino, J. M. (2012). EPR Study of Charge Separation Within Novel Brookite TiO_2 photocatalysts for the conversion of CO_2 to Fuels, Abstr. Pap. Am. Chem. Soc., Volume 244, Paper 468-ENFL.

23. Quevedo, J. A., Omosebi, A., Pfeffer, R. (2010). Fluidization Enhancement of Agglomerates of Metal Oxide Nanopowders by Microjets. Aiche Journal, 56, 1456-1468.

24. Pfeffer, R., Quevedo, J. A., Flesch, J. (2012). Fluidized bed systems and methods including micro-jet flow. United States Patent No. US 8118243 B2.

25. Wang, S. Y., Shao, B. L., Li, X. Y., Zhao, J., Liu, L. L., Liu, Y. K., Liu, Y., Dong, Q. (2017). Simulations of vertical jet penetration using a filtered two-fluid model in a gas-solid fluidized bed. Particuology, 31, 95-104.

26. Martin, R., Tilman J. S., Serge, M. A. B., Ruud van Ommen, J. (2012). Scale-up of bubbling fluidized bed reactors - A review. Powder Technology, 217, 21-38.

27. Wang, Y., Wang, T. J., Yang, Y., Jin, Y. (2002). Resonance characteristics of a vibrated fluidized bed with a high bed hold-up. Powder Technology, 127, 196-202.

28. Valverde, J. M., Castellanos, A., Quintanilla, M. A. S. (2001). Effect of vibration on the stability of a gas-fluidized bed of fine powder. Physical Review E, 64.

29. Clift, R., Filla, M., Massimilla, L. (1976). Gas and particle motion in jets in fluidized beds. International Journal of Multiphase Flow, 2, 549-561.

30. Hong, R., Li, H., Li, H., Wang, Y. (1997). Studies on the inclined jet penetration length in a gas solid fluidized bed. Powder Technology, 92, 205-212.

31. Hong, R. Y., Guo, Q. J., Luo, G. H., Zhang, J. Y., Ding, J. (2003). On the jet penetration height in fluidized beds with two vertical jets. Powder Technology, 133, 216-227.

32. Chyang, C. S., Chang, C. H., Chang, J. H. (1997). Gas discharge modes at a single horizontal nozzle in a two-dimensional fluidized bed. Powder Technology, 90, 71-77.

33. Vaccaro, S. (1997). Analysis of the variables controlling gas jet expansion angles in fluidized beds. Powder Technology, 92, 213-222.

34. Hong, R., Ding, J., Li, H. (2005). Fluidization of fine powders in fluidized beds with an upward or a downward air jet. China Particuology, 3, 181-186.

35. Ward-Smith A. J. (1979). Critical flowmetering: the characteristics of cylindrical nozzles with sharp upstream edges. Int J Heat Fluid Flow, 1, 123–132.

36. Yao, W., Guangsheng., G., Fei, W., Jun, W. (2002). Fluidization and agglomerate structure of SiO_2 nanoparticles. Powder Technology, 124, 152-159.

37. Nam, C., Pfeffer, R., Dave, R., Sundaresan, S. (2004). Aerated vibrofluidization of silica nanoparticles. AIChE Journal, 50, 1776-1785.

38. Zhang, W., & Zhao, M. (2010). Fluidisation behaviour of silica nanoparticles under horizontal vibration. Journal of Experimental Nanoscience, 5, 69–82.

39. Wank, J. R., George, S. M., Weimer, A. W. (2001). Vibro-fluidization of fine boron nitride powder at low pressure. Powder Technology, 121, 195–204.

40. Pope S. B. (2000). Turbulent Flows: Free Shear Flows. Cambridge University Press.

41. Chen, X., &Wang, J. (2014). A comparison of two-fluid model, dense discrete particle model and CFD-DEM method for modeling impinging gas–solid flows. Powder Technology, 254, 94-102.

42. Acosta-Iborra, A., Hernandez J. F., de Vega, M., Briongos, J. V. (2012). A novel methodology for simulating vibrated fluidized beds using two-fluid models. Chemical Engineering Journal, 198–199, 261–274.

43. Van Wachem, B. G. M., & Almstedt, A. E. (2003). Methods for multiphase computational fluid dynamics. Chemical Engineering Journal, 96, 81–98.

44. Gidaspow, D. (1994). Multiphase Flow and Fluidization. Academic Press, Boston.

45. Hernández-Jiménez, F., Sánchez-Delgado, S., Gómez-García, A., Acosta-Iborra, A. (2011). Comparison between two-fluid model simulations and particle image analysis & velocimetry (PIV) results for a two-dimensional gas–solid fluidized bed. Chem. Eng. Sci., 66, 3753–3772.

46. Hernández-Jiménez, F., Third, J. R., Acosta-Iborra, A., Müller, C. R. (2011). Comparison of bubble eruption models with two-fluid simulations in a 2D gas-fluidized bed. Chem. Eng. J., 171, 328–339.

47. Fabre, A. (2016). Fluidized nanoparticle agglomerates formation, characterization and dynamics. PhD thesis, Delft University of Technology.

48. Jop, P., Forterre, Y., Pouliquen, O. (2006). A constitutive law for dense granular flows. Nature, 441, 727–730.

49. Schneiderbauer, S., Aigner, A., Pirker, S. (2012). A comprehensive frictional-kinetic model for gas–particle flows: Analysis of fluidized and moving bed regimes. Chem. Eng. Sci., 80, 279–292.

50. Schaeffer, D. G. (1987). Instability in the Evolution Equations Describing Incompressible Granular Flow. Journal of Differential Equations, 66, 19-50.

51. Schaeffer, D. G., Pitman, E.B. (1988). Ill-Posedness in Three-Dimensional Plastic Flow. Comm. Pure Appl. Math., 41, 879-890.

52. Pleite, E. C., Jiménez, F. H., Iborra, A. A. (2015). Compressible-gas two-fluid modeling of isolated bubbles in a vertically vibrated fluidized bed and comparison with experiments, Chemical Engineering Journal, 271, 287–299.

53. Taghipour, F., Ellis, N., Wong, C. (2005). Experimental and Computational Study of Gas-Solid Fluidized Bed Hydrodynamics. Chemical Engineering Science Journal, 60, 6857-6867.

54. Sinclair, J. L., & Jackson, R., (1989). Gas-particle flow in a vertical pipe with particle-particle interactions. AIChE Journal, 35, 1473–1496.

55. Pain, C., Mansoorzadeh, S., Oliveira, C. R. E. D., Goddard, A. J. H. (2001). Numerical Modeling of Gas-Solid Fluidized Beds Using the Two-Fluid Approach. International Journal for Numerical Methods in Fluids, 36, 91–124.

56. Solli, K. A., & Agu, C. (2017). Evaluation of drag models for CFD simulation of fluidized bed biomass gasification. Proceedings of the 58th SIMS, Reykjavik, Iceland.

57. An, K., Andino, J. M. (2019). Enhanced fluidization of nanosized TiO_2 by a microjet and vibration assisted (MVA) method. Powder Technology, 356, 200-207.

58. De Bertodano, M. L., Fullmer, W., Clausse, A., Ransom, V. (2017). Two-Fluid Model Stability. Simulation and Chaos, Springer International Publishing.

59. Ansari, M. R., & Shokri, V. (2011). Numerical modeling of slug flow initiation in a horizontal channelsusing a two-fluid model. International journal of Heat and Fluid flow, 32, 145-155.

60. Zhou, T., & Hongzhong, L. (1999). Estimation of agglomerate size for cohesive particles during fluidization. Powder Technology, 101, 57-62.

61. Mohammad, R., Katia. B., Maryam. T., Navid. M. M. (2016). Size of Nanoparticle Agglomerates in Fluidization. The canadian journal of chemical engineering, 94, 476-484.

62. Dahneke, B. (1972). The influence of flattening on the adhesion of particles. Journal of Colloid and Interface Science, 40, 1.

63. Krupp, H. (1967). Particle adhesion theory and experiment. Advances in Colloid and Interface Science, 1, 111-239.

64. Butt, H. J., & Kappl, M. (2010). Surface and Interfacial Forces. Wiley.

65. Kendall, K., Alford, N. M., Birchall, J. D. (1987). Elasticity of particle assemblies as a measure of the surface energy of solids. Proceedings of the Royal Society of London A: Mathematical, Physical and Engineering Sciences, 412, 269.

66. Kendall, K., & Weihs, T. P. (1993). Adhesion of nanoparticles within spray dried agglomerates. Journal of Physics D: Applied Physics, 25, A.

67. Timoshenko, S. P., Goodier, J. N. (1970). Theory of Elasticity, McGraw-Hill.

68. Zhou, T., Li, H. (2000). Force balance modeling for agglomerating fluidization of cohesive particles. Powder Technology, 111, 60-65.

69. Horio, M., & Iwadate, Y. (1996). The prediction of sizes of agglomerates formed in fluidized beds. Proceedings of the 5thWorld Congress of Chemical Engineering, 2nd Intl. Particle Technology Forum, 5, 571.

70. Darton, R. C., La Nauze, R. D., Davidson, J. F., Harrison, D. (1977). Bubble growth due to coalescence in fluidized beds. Trans. Inst. Chem. Eng., 55, 274–280.

71. Farshi, A., Javaherizadeh, H. and Hamzavi-Abedi, M. A. (2008). An investigation of the effect of bubble diameter on the performance of gas solid fluidized bed reactor and two phase modeling of bubbling fluidized bed reactor in melamine production. Petroleum & Coal, 50, 11–22.

72. Mori, S., & Wen, C. Y. (1975). Estimation of bubble diameter in gaseous fluidized beds. AIChE J., 21, 109–115.

73. Rowe, P. N. (1976). Prediction of bubble size in gas fluidized bed. Chem. Eng. Sci., 31, 285–288.

74. Yasui, G., & Johanson, L. N. (1958). Characteristics of gas pockets in fluidized beds. AIChE J., 4, 445.

75. Park, W. H., Kang, W. K., Copes, C. E., Osberg, G. L. (1969). The properties of bubbles in fluidized beds of conducting particles as measured by an electro resistivity probe. Chem. Eng. Sci., 24, 851.

76. Kato, K., & Wen, C. Y. (1969). Bubble assemblage, model for fluidized bed catalytic reactors. Chem. Eng. Sci., 24, 1351-1369.

77. Guo, Q., Yang, X., Shen, W., Liu, H. (2007). Agglomerate size in an acoustic fluidized bed with sound assistance. Chemical Engineering and Processing: Process Intensification, 46, 307.

78. Zhou, T., Li, H., Shinohara, K. (2006). Agglomerating fluidization of group C particles: major factors of coalescence and breakup of agglomerates. Advanced Powder Technol., 17, 159–166.

79. Leva, M. (1959). Fluidization, McGraw-Hill Book, New York.

80. Fabre, A., Clemente, A., Balas, F., Pilar Lobera M., Santamaría, J., Kreutzera, M. T., van Ommen, J. R. (2017) Modeling the size distribution in a fluidized bed of nanopowder. Environ. Sci.: Nano, 4, 670-678.

81. Li, L., Li, Y., Wen, X., Wang, F., Zhao, N., Xiao, F., Wei, W., Sun, Y. (2011). CO_2 Capture over $K2CO_3/MgO/Al_2O_3$ Dry Sorbent in a Fluidized Bed. Energy Fuels, 25, 3835-3842.

82. Li, L., King, D. L., Nie, Z., Li, X. S., Howard, C. (2010). $MgAl_2O_4$ spinel-stabilized calcium oxide absorbents with improved durability for high-temperature CO_2 capture. Energy Fuels, 24, 3698–3703.

83. Lu, H., Smirniotis, P. G., Ernst, F. O., Pratsinis, S. E. (2009). Nanostructured Ca-based sorbents with high CO_2 uptake efficiency. Chem Eng Sci., 64, 1936–1943.

84. Valverde, J.M., Pontiga, F., Soria Hoyo, C., Quintanilla, M. A. S., Moreno H., Duran, F. J., Espin, M.J. (2011). Improving the gas-solids contact efficiency in a fluidized bed of CO_2 adsorbent fine particles. Phys Chem Chem Phys., 13, 14906-14909.

85. Seo, Y., Jo, S. H., Ryu, C. K., Yi, C. K. (2009). Effect of reaction temperature on CO_2 capture using potassium-based solid sorbent in bubbling fluidized-bed reactor. J. Environ. Eng., 135, 473−477.

86. Lee, S. C., Chae, H. J., Lee, S. J., Park, Y. H., Ryu, C. K., Yi, C. K.; Kim, J. C. (2009). Novel regenerable potassium-based dry sorbents for CO_2 capture at low temperatures. J. Mol. Catal., 56, 179−184.

87. Zhao, C., Chen, X., Zhao, C. (2009). CO_2 absorption using dry potassium-based sorbents with different supports. Energy Fuels, 23, 4683−4687.

88. Lee, S. C., Chae, H. J., Lee, S. J., Choi, B. Y., Yi, C. K., Lee, J. B., Ryu, C. K., Kim, J. C. (2008). Development of regenerable MgO-based sorbent promoted with K_2CO_3 for CO_2 capture at low temperatures. Environ. Sci. Technol., 42, 2736−2741.

89. Zhao, C., Chen, X., Zhao, C., Wu, Y., Dong, W. (2012). K_2CO_3/Al_2O_3 for capturing CO_2 in flue gas from power plants. Part 3: CO_2 capture behaviors of K_2CO_3/Al_2O_3 in a bubbling fluidized-bed reactor. Energy Fuels, 26, 3062−3068.

90. Yi, C. K., Jo, S. H., Seo, Y. (2008). The effect of voidage on the CO_2 sorption capacity of K-based sorbent in a dual circulating fluidized bed process. J. Chem. Eng. Jpn., 41, 691-694.

91. Li, L., Li, Y., Wen, X., Wang, F., Zhao, N., Xiao, F., Wei, W., Sun, Y. (2011). CO_2 capture over $K_2CO_3/MgO/Al_2O_3$ dry sorbent in a fluidized bed. Energy Fuels, 25,

3835−3842.

92. Vincenzo, V., Diana, S., Paolo, C. (2015). Steam Reduction of CO_2 in a Photocatalytic Fluidized Bed Reactor. Chemical Engineering Transactions, 43, 1003-1008.

93. Veneman, R., Li, Z. S., Hogendoorn, J. A., Kersten, S. R. A., Brilman, D. W. F. (2012). Continuous CO_2 capture in a circulating fluidized bed using supported amine sorbents. Chemical Engineering Journal, 207-208, 18–26.

94. Yu, W., Wang, T., Park, A., Fang, M. (2019) Review of liquid nano-absorbents for enhanced CO_2 capture. Nanoscale, 11, 17137-17156.

95. Hornbostel, K., Nguyen, D., Bourcier, W., Knipe, J., Worthington, M., McCoy, S., Stolaroff, J. (2019). Packed and fluidized bed absorber modeling for carbon capture with microencapsulated sodium carbonate solution. Applied Energy, 235, 1192-1204.

APPENDIX A

DATA FOR THE CHARTS AND FIGURES IN CHAPTER 2

Table A.1. Amplitude versus Frequency Domain of the Experimental Setup in Figure 2

Frequency [Hz]	Amplitude [mm]	Frequency [Hz]	Amplitude [mm]
40	0.1115	56	0.1745
42	0.1525	58	0.1275
44	0.1315	59	0.0565
46	0.126	59.5	0.052
48	0.1405	60	0.047
49	0.1925	60.5	0.047
49.5	0.199	61	0.055
50	0.2265	62	0.093
50.5	0.2285	63	0.141
51	0.23	64	0.14
51.5	0.219	66	0.1495
52	0.2	68	0.123
53	0.1685	69	0.1195
54	0.1565	70	0.109

Table A.2. Nondimensional Height as a Function of Vibration Intensity at Different Frequencies, 50, 60 and 70 Hz in the MVA System in Figure 4

TiO_2 P25			TiO_2 P90		
Frequency [Hz]	Vibrational Intensity, Γ	H/H_0	Frequency [Hz]	Vibrational Intensity, Γ	H/H_0

50	1	4.37	50	1	5.81
50	1.2	4.45	50	1.2	5.95
50	1.4	4.55	50	1.4	6.9
50	1.6	4.97	50	1.6	7.12
50	1.8	5	50	1.8	7.16
50	2.0	5.05	50	2.0	7.16
60	1	3.72	60	1	5.06
60	1.2	3.77	60	1.2	5.1
60	1.4	3.81	60	1.4	5.13
60	1.6	4.1	60	1.6	5.14
70	1	4.26	70	1	5.53
70	1.2	4.31	70	1.2	5.72
70	1.4	4.46	70	1.4	6
70	1.6	4.45	70	1.6	6.3
70	1.8	4.47	70	1.8	6.4
70	2.0	4.55	70	2.0	6.4

Table A.3. Nondimensional Height as a Function of Frequency at Different Gas Velocities in Figure 5

TiO_2 P25			TiO_2 P90		
Gas velocity [m/s]	Frequency [Hz]	H/H_0	Gas velocity [m/s]	Frequency [Hz]	H/H_0
0.01	40	3.78	0.01	40	6
0.01	45	4.12	0.01	45	6.33
0.01	50	4.18	0.01	50	6.45
0.01	55	4.1	0.01	55	6.07
0.01	60	3.11	0.01	60	5.39
0.01	65	3.71	0.01	65	5.75

0.01	70	3.81	0.01	70	5.73
0.02	40	4.85	0.02	40	6.3
0.02	45	4.78	0.02	45	6.6
0.02	50	5.08	0.02	50	7.06
0.02	55	4.4	0.02	55	6.85
0.02	60	4	0.02	60	5.69
0.02	65	4.22	0.02	65	6.3
0.02	70	4.36	0.02	70	6.2

Table A.4. Nondimensional Height of TiO_2 P25 as a Function of Superficial Gas Velocity for a Frequency of 50 Hz and a Vibrational Intensity of 1.6 in Figure 6

Gas Velocity [m/s]	Nondimensional Height, H/H_0	
	VFB	MVA
0.001	1.21	1.24
0.002	1.26	1.31
0.003	1.34	1.36
0.004	1.36	1.39
0.005	1.39	1.43
0.006	1.41	1.56
0.007	1.41	2.31
0.008	1.41	3.41
0.009	1.46	3.82
0.01	1.53	4.07
0.011	1.56	4.17

0.012	2.07	4.29
0.013	2.14	4.31
0.014	2.24	4.46
0.015	2.34	4.51
0.016	2.58	4.63
0.017	2.65	4.78
0.019	2.73	4.95
0.021	2.9	4.97
0.023	2.91	5.07
0.025	3	5.12
0.027	2.89	5.13
0.029	2.93	5.15
0.031	2.92	5.12
0.033	2.92	5.09

Table A.5. Nondimensional Height as a Function of Gas Velocity in the MVA System for TiO_2 P25 and TiO_2 P90 Nanopowders in Figure 7

Gas Velocity [m/s]	Nondimensional Height, H/H_0	
	TiO_2 P25	TiO_2 P90
0.001	1.24	1.1
0.002	1.31	1.24
0.003	1.36	1.4

0.004	1.39	1.88
0.005	1.43	2.08
0.006	1.56	2.32
0.007	2.31	2.6
0.008	3.41	2.78
0.009	3.82	3
0.01	4.07	3.3
0.011	4.17	3.4
0.012	4.29	3.6
0.013	4.31	5
0.014	4.46	5.2
0.015	4.51	5.4
0.016	4.63	5.56
0.017	4.78	7.1
0.019	4.95	7.12
0.021	4.97	7.1
0.023	5.07	6.98
0.025	5.12	6.61
0.027	5.13	6.38
0.029	5.15	6.05
0.031	5.12	5.86
0.033	5.09	5.82

Table A.6. Nondimensional Height as a Function of Fluidization Time in Figure 8

Time [seconds]	Nondimensional Height, H/H_0	
	TiO_2 P25	TiO_2 P90
1	1.04	1.07
3	1.17	1.19
5	1.21	1.26
7	1.34	1.31
9	1.34	1.36
11	1.29	1.34
13	1.34	1.43
15	1.41	1.46
17	1.43	1.58
19	1.46	1.68
21	1.56	1.75
31	1.82	2.65
41	3.53	3.31
51	4.75	4.56
61	4.95	5.58
71	4.74	5.82
81	4.68	5.85
91	5	6.21

100	5	6.46
200	5.04	7.19
300	5	7.17
400	4.92	7.12
500	4.95	7.19
800	4.97	7.19
1000	4.97	7.14
1200	4.97	7.19
1500	4.95	7.24
1900	4.96	7.21

Table A.7. Experimental Result of Outlet Velocity of the Micronozzle at Different Upstream Pressures in Figure 9

Upstream Pressure [psig]	Outlet gas velocity [m/s]
1	83.77
5	198.53
10	263.03
15	314.1
20	315.22
25	323.1
30	319.31
40	325.74

50	328.02
60	325.63
70	330.42
80	330.99
90	334.13
100	327.77

Table A.8. Nondimensional Height of TiO_2 P25 Powder as a Function of Vibrational Intensity at Different Upstream Pressures through the Microjet in Figure 10

Upstream Pressure [psig]	Vibrational Intensity, Γ	Nondimensional Height, H/H_0
5	1	4.58
5	1.2	4.77
5	1.4	4.84
5	1.6	4.95
5	1.8	4.98
5	2	4.98
10	1	4.57
10	1.2	4.72
10	1.4	4.76
10	1.6	4.84

10	1.8	4.87
10	2	4.89
15	1	4.57
15	1.2	4.64
15	1.4	4.71
15	1.6	4.79
15	1.8	4.86
15	2	4.89
20	1	4.56
20	1.2	4.63
20	1.4	4.71
20	1.6	4.72
20	1.8	4.77
20	2	4.83
25	1	4.48
25	1.2	4.55
25	1.4	4.63
25	1.6	4.65
25	1.8	4.74
25	2	4.79
30	1	4.33
30	1.2	4.48

30	1.4	4.56
30	1.6	4.66
30	1.8	4.69
30	2	4.76

Table A.9. Bed Expansion Behavior of TiO_2 in MVA System in Figure 11

Gas velocity [m/s]	Vibrational Intensity	Nondimensional Height [H/H_0]	
		P25	P90
0.001	1.2	1.18	1.06
0.002	1.2	1.25	1.16
0.003	1.2	1.27	1.31
0.004	1.2	1.29	1.41
0.005	1.2	1.36	1.45
0.006	1.2	1.61	1.66
0.007	1.2	1.75	1.83
0.008	1.2	2.0	2.04
0.009	1.2	2.29	2.5
0.01	1.2	2.72	3.22
0.011	1.2	2.88	3.83
0.012	1.2	2.95	4.06
0.013	1.2	3.06	4.27
0.014	1.2	3.20	4.45
0.015	1.2	3.38	4.58
0.016	1.2	3.43	5.0
0.017	1.2	3.52	5.18
0.019	1.2	3.65	5.33

0.021	1.2	3.75	6.27
0.023	1.2	3.84	6.68
0.025	1.2	3.97	6.68
0.027	1.2	4.06	6.66
0.029	1.2	4.11	5.93
0.031	1.2	4.13	5.91
0.033	1.2	4.15	5.93
0.001	1.4	1.18	1.06
0.002	1.4	1.22	1.14
0.003	1.4	1.25	1.33
0.004	1.4	1.29	1.41
0.005	1.4	1.6	1.5
0.006	1.4	1.79	1.81
0.007	1.4	2.06	2.06
0.008	1.4	2.45	2.25
0.009	1.4	3.4	2.6
0.01	1.4	3.52	3.33
0.011	1.4	3.65	4.12
0.012	1.4	3.75	4.2
0.013	1.4	3.84	4.37
0.014	1.4	3.86	4.68
0.015	1.4	3.8	5.1
0.016	1.4	3.9	5.31
0.017	1.4	3.97	5.72
0.019	1.4	4.06	6.16
0.021	1.4	4.09	6.89
0.023	1.4	4.04	6.72
0.025	1.4	4.09	6.91

0.027	1.4	4.13	6.83
0.029	1.4	4.27	6.1
0.031	1.4	4.25	6.1
0.033	1.4	4.29	6.06
0.001	1.6	1.15	1.08
0.002	1.6	1.22	1.22
0.003	1.6	1.27	1.45
0.004	1.6	1.29	1.89
0.005	1.6	1.34	2.08
0.006	1.6	1.45	2.7
0.007	1.6	2.15	3.35
0.008	1.6	3.18	3.6
0.009	1.6	3.56	3.83
0.01	1.6	3.79	4.06
0.011	1.6	3.88	4.29
0.012	1.6	4.0	4.6
0.013	1.6	4.02	5.12
0.014	1.6	4.15	5.45
0.015	1.6	4.2	5.64
0.016	1.6	4.31	5.72
0.017	1.6	4.45	6.87
0.019	1.6	4.61	7.25
0.021	1.6	4.63	7.31
0.023	1.6	4.72	7.29
0.025	1.6	4.77	7.16
0.027	1.6	4.78	7.08
0.029	1.6	4.8	6.47
0.031	1.6	4.77	6.29

0.033	1.6	4.75	6.27
0.001	1.8	1.18	1.08
0.002	1.8	1.25	1.22
0.003	1.8	1.25	1.45
0.004	1.8	1.27	1.89
0.005	1.8	1.29	2.08
0.006	1.8	1.43	2.7
0.007	1.8	2.0	3.35
0.008	1.8	3.18	3.6
0.009	1.8	3.63	3.83
0.01	1.8	3.79	4.06
0.011	1.8	3.86	4.29
0.012	1.8	3.97	4.6
0.013	1.8	3.98	5.12
0.014	1.8	4.15	5.45
0.015	1.8	4.22	5.64
0.016	1.8	4.27	5.72
0.017	1.8	4.43	6.87
0.019	1.8	4.59	7.25
0.021	1.8	4.77	7.31
0.023	1.8	4.77	7.29
0.025	1.8	4.72	7.16
0.027	1.8	4.77	7.08
0.029	1.8	4.77	6.47
0.031	1.8	4.72	6.29
0.033	1.8	4.75	6.27
0.001	2.0	1.2	1.06
0.002	2.0	1.29	1.25

0.003	2.0	1.31	1.39
0.004	2.0	1.36	1.87
0.005	2.0	1.4	2.06
0.006	2.0	1.47	2.6
0.007	2.0	1.81	2.62
0.008	2.0	3.09	2.83
0.009	2.0	3.52	3.77
0.01	2.0	3.61	3.97
0.011	2.0	3.79	4.16
0.012	2.0	3.93	4.64
0.013	2.0	3.97	5.1
0.014	2.0	4.09	5.31
0.015	2.0	4.13	5.62
0.016	2.0	4.2	5.75
0.017	2.0	4.4	7.08
0.019	2.0	4.54	7.18
0.021	2.0	4.65	7.25
0.023	2.0	4.77	7.27
0.025	2.0	4.77	7.18
0.027	2.0	4.79	6.66
0.029	2.0	4.72	6.35
0.031	2.0	4.75	6.45
0.033	2.0	4.77	6.25

Table A.10. 9 Sample Data Points in Figure 11

Gas velocity [m/s]	Vibrational Intensity	Nondimensional Height [H/H_0]	
		P25	P90

0.01	1.3	14.63	19.36
0.02	1.3	18.0	29.1
0.03	1.3	19.13	32.03
0.01	1.5	14.5	20.6
0.02	1.5	18.8	30.86
0.03	1.5	19.96	34.63
0.01	1.7	15.13	21.3
0.02	1.7	19.5	32.5
0.03	1.7	19.93	30.9

Table A.11. Error Percent from 9 Sampling Points in Figure 12

Sample number	% Error	
	TiO_2 P25	TiO_2 P90
1	5.34	2.87
2	-10.37	-2.56
3	-4.58	4.07
4	-2.85	-0.46
5	-12.76	-2.85
6	-8.24	6.14
7	-2.28	-1.52
8	-13.00	-0.36
9	-13.97	-7.84

Table A.12. Nondimensional Pressure Drop as a Function of Gas Velocity in Figure 13

Gas velocity [m/s]	Nondimensional Pressure drop			
	TiO_2 P25		TiO_2 P90	
	MVA	VFB	MVA	VFB
0.001	-	0.27	-	0.13
0.002	-	0.27	-	0.20
0.003	-	0.34	-	0.27
0.004	-	0.41	-	0.34
0.005	0.68	0.48	-	0.48
0.006	0.82	0.54	0.51	0.48
0.007	0.82	0.54	0.68	0.48
0.008	0.89	0.61	0.75	0.54
0.009	0.96	0.68	0.82	0.54
0.01	0.96	0.75	0.96	0.68
0.011	0.96	0.82	0.96	0.75
0.012	0.96	0.82	0.96	0.82
0.013	0.96	0.82	0.96	0.82
0.014	0.96	0.82	0.96	0.82
0.015	0.96	0.82	0.96	0.82
0.016	0.96	0.82	0.96	0.82
0.017	0.96	0.82	0.96	0.82

0.019	0.96	0.82	0.96	0.82
0.021	0.96	0.82	0.96	0.82
0.023	0.96	0.82	0.96	0.82
0.025	0.96	0.82	0.96	0.82
0.027	0.96	0.82	0.96	0.82
0.029	0.96	0.82	0.96	0.82
0.031	0.96	0.82	0.96	0.82
0.033	0.96	0.82	0.96	0.82

APPENDIX B

DATA FOR THE CHARTS AND FIGURES IN CHAPTER 3

Table B.1. MVA Fluidized Bed Height over Time in Figure 16

Time [seconds]	Nondimensional Height, H/H_0	
	Experiment	TFM simulation
1	1.21	1.3
2	1.19	1.56
3	1.39	1.85
4	1.56	1.92
5	1.62	2.15
6	1.8	2.3
8	1.95	2.37
10	2.18	2.52
12	2.3	2.76
14	2.46	2.89
16	2.53	3.07
18	2.66	3.16
20	2.75	3.21
22	3.1	3.38
24	3.23	3.36
26	3.29	3.43
28	3.39	3.51
30	3.48	3.65
32	3.68	3.75

34	3.89	3.79
36	4.03	3.91
38	4.04	3.95
40	4.08	4.06
42	4.17	4.17
44	4.22	4.23
46	4.28	4.47
48	4.39	4.52
50	4.43	4.56
52	4.54	4.61
54	4.62	4.62
56	4.66	4.61
58	4.72	4.6
60	4.82	4.65
62	4.85	4.68
64	4.84	4.71
66	4.88	4.7
68	4.91	4.75
70	4.88	4.79
72	4.92	4.78
74	4.9	4.72
76	4.86	4.8

78	4.9	4.81
80	4.86	4.8
82	4.87	4.81
84	4.89	4.8
86	4.9	4.8
88	4.89	4.78
90	4.87	4.74

Table B.2. Gas Velocity Distribution in the MVA System under Condition of U_g= 0.03 m/s, f= 50 Hz and A= 0.016 mm in Figure 17

0.086327	0.185377	0.133003	0.147614	0.168443	0.104087
0.156199	0.266919	0.159085	0.15947	0.28537	0.190156
0.181209	0.254633	0.146205	0.122439	0.275144	0.201187
0.221292	0.25127	0.121069	0.1144	0.257835	0.239416
0.258191	0.253148	0.117869	0.114609	0.280326	0.27891
0.286463	0.29606	0.160111	0.145003	0.346386	0.301167
0.290428	0.328268	0.179444	0.159638	0.363296	0.307849
0.291296	0.266843	0.117325	0.127474	0.309466	0.295359
0.27742	0.291816	0.107353	0.119932	0.310135	0.283212
0.262044	0.298505	0.103372	0.104382	0.318049	0.280019
0.250957	0.301851	0.111737	0.108961	0.318478	0.275144
0.237758	0.300204	0.121443	0.124855	0.310593	0.272584
0.229912	0.290779	0.14203	0.121523	0.298376	0.276877
0.218769	0.275268	0.157893	0.11714	0.288007	0.27057
0.206828	0.263153	0.160302	0.120868	0.280829	0.256
0.196244	0.263338	0.162841	0.127666	0.275971	0.238605
0.190688	0.266767	0.163503	0.133364	0.27703	0.229634
0.195004	0.264227	0.156875	0.141296	0.278468	0.222152
0.199167	0.260518	0.154669	0.140987	0.2693	0.213868
0.194355	0.258856	0.154330	0.136324	0.259402	0.206416
0.186481	0.262016	0.157103	0.136469	0.25447	0.198916
0.181172	0.265317	0.162048	0.135538	0.252774	0.189316
0.177347	0.259666	0.167009	0.132296	0.250114	0.186702

0.169265	0.254974	0.173642	0.138667	0.245458	0.179271
0.150668	0.252954	0.180430	0.149291	0.242249	0.182021
0.147262	0.246047	0.184586	0.155881	0.231943	0.181252
0.142056	0.239325	0.187478	0.152101	0.221114	0.172937
0.132375	0.233217	0.186948	0.150341	0.216482	0.162235
0.127293	0.228445	0.182568	0.159186	0.215521	0.158403
0.13278	0.223728	0.181945	0.16237	0.211605	0.160532
0.130448	0.218507	0.181621	0.159639	0.205061	0.158955
0.124809	0.210304	0.178432	0.157767	0.19705	0.155989
0.120265	0.200648	0.171937	0.152955	0.185312	0.154968
0.118043	0.185994	0.164097	0.145987	0.174935	0.148767
0.109969	0.171744	0.155069	0.139703	0.167446	0.135318
0.102609	0.156364	0.142277	0.135558	0.16081	0.124431
0.093182	0.142509	0.131233	0.132057	0.1548	0.119352
0.090653	0.136233	0.127943	0.122742	0.148622	0.116355
0.088617	0.131948	0.122126	0.115182	0.144094	0.105486
0.080732	0.123705	0.115640	0.111758	0.133062	0.090845
0.069343	0.111993	0.113596	0.107014	0.117472	0.076032
0.058954	0.100909	0.114635	0.099903	0.099923	0.066853
0.058329	0.088104	0.113578	0.095442	0.088541	0.063149
0.060939	0.077494	0.100126	0.084252	0.080339	0.061816
0.066986	0.067631	0.08338	0.069353	0.073852	0.061181
0.065537	0.057024	0.067006	0.055968	0.058359	0.054954
0.049623	0.039974	0.049570	0.044339	0.041415	0.044882

Table B.3. Agglomerate Size Distribution in the MVA System based on the Simulation Work in Figure 20

73.52	60.24	65.6	63.86	61.74	69.94
62.94	54.96	62.64	62.6	54.06	59.86
60.6	55.62	64.02	67.02	54.54	59.02
57.62	55.8	67.22	68.22	55.44	56.48
55.42	55.7	67.7	68.2	54.3	54.36
54	53.56	62.54	64.16	51.5	53.34
53.82	52.2	60.74	62.58	50.9	53.04
53.78	54.96	67.78	66.32	52.98	53.6
54.44	53.76	69.38	67.38	52.94	54.16
55.22	53.46	70.06	69.88	52.62	54.3
55.82	53.3	68.64	69.1	52.6	54.54
56.58	53.38	67.16	66.68	52.92	54.68

57.06	53.8	64.5	67.16	53.46	54.46
57.78	54.54	62.76	67.8	53.92	54.78
58.6	55.16	62.52	67.26	54.28	55.54
59.38	55.14	62.28	66.3	54.5	56.54
59.82	54.98	62.2	65.56	54.46	57.08
59.48	55.1	62.86	64.58	54.38	57.56
59.16	55.3	63.1	64.62	54.84	58.1
59.54	55.38	63.14	65.18	55.36	58.64
60.16	55.22	62.84	65.16	55.62	59.18
60.6	55.04	62.34	65.28	55.72	59.92
60.94	55.34	61.88	65.68	55.86	60.14
61.66	55.6	61.26	64.9	56.12	60.76
63.52	55.7	60.66	63.68	56.32	60.52
63.9	56.1	60.32	62.98	56.94	60.6
64.5	56.48	60.08	63.36	57.62	61.32
65.68	56.86	60.12	63.56	57.94	62.34
66.36	57.16	60.48	62.64	58	62.72
65.62	57.46	60.54	62.32	58.26	62.5
65.92	57.8	60.56	62.58	58.72	62.66
66.7	58.36	60.84	62.78	59.32	62.96
67.34	59.06	61.42	63.28	60.26	63.06
67.66	60.2	62.14	64.04	61.14	63.74
68.94	61.44	63.06	64.78	61.82	65.3
70.2	62.92	64.46	65.28	62.48	66.74
72.02	64.44	65.82	65.72	63.08	67.48
72.56	65.2	66.26	66.98	63.74	67.92
73	65.74	67.06	68.1	64.26	69.7
74.86	66.84	68.04	68.64	65.6	72.52
78.06	68.6	68.36	69.44	67.76	76.1
81.68	70.52	68.18	70.7	70.7	78.84
81.94	73.12	68.36	71.56	73.02	80.12
80.92	75.7	70.66	74	74.96	80.6
78.8	78.6	74.2	78.04	76.7	80.84
79.28	82.46	78.8	82.92	81.92	83.36
85.86	91.66	85.9	88.8	90.66	88.48

Table B.4. Averaged Values of (a) Gas Velocity and (b) Agglomerate Size at each Row up to Nondimensional Height, H/H_0=5 in Figure 22

Nondimensional Height, H/H_0	Gas velocity [m/s]	Agglomerate size [μm]
0	0.137475	65.81667
0.10	0.202867	59.51
0.21	0.196803	60.13667
0.32	0.20088	60.13
0.43	0.217176	59.28
0.54	0.255865	56.51667
0.65	0.271487	55.54667
0.76	0.234627	58.23667
0.86	0.231645	58.67667
0.97	0.227729	59.25667
1.08	0.227855	59
1.19	0.227906	58.56667
1.30	0.226584	58.40667
1.41	0.221274	58.59667
1.52	0.214663	58.89333
1.63	0.210778	59.02333
1.73	0.210165	59.01667
1.84	0.209671	58.99333
1.95	0.206418	59.18667
2.06	0.201614	59.54
2.17	0.199243	59.69667
2.28	0.197694	59.81667
2.39	0.195522	59.97333
2.5	0.193546	60.05
2.60	0.192936	60.06667
2.71	0.191162	60.14
2.82	0.185835	60.56
2.93	0.180266	61.08333
3.04	0.178569	61.22667
3.15	0.178827	61.11667
3.26	0.175705	61.37333
3.36	0.170725	61.82667
3.47	0.164348	62.40333
3.58	0.156304	63.15333
3.69	0.146541	64.22333

3.80	0.137008	65.34667
3.91	0.128855	66.42667
4.02	0.123758	67.11
4.13	0.117909	67.97667
4.23	0.10929	69.41667
4.34	0.099242	71.38667
4.45	0.090196	73.43667
4.56	0.084524	74.68667
4.67	0.077495	76.14
4.78	0.070398	77.86333
4.89	0.059808	81.45667
5	0.044967	88.56

Table B.5. Breakthrough Curves of CO_2 on TiO_2 Sorbent in VFB and MVA Fluidization Systems in Figure 27

Time [minutes]	C_{out}/C_{in}, MVA	C_{out}/C_{in}, VFB
0.01	0	0
0.05	0	0
0.08	0	0
0.11	0	0
0.15	0	0
0.18	0	0
0.21	0	0
0.25	0	0.007
0.28	0	0.009
0.31	0	0.012
0.35	0	0.019
0.38	0	0.025
0.41	0	0.036
0.45	0	0.049
0.48	0	0.071
0.51	0	0.1
0.55	0.004	0.141
0.58	0.016	0.172
0.61	0.047	0.229
0.65	0.064	0.27
0.68	0.1	0.301
0.71	0.12	0.331
0.75	0.164	0.35

0.78	0.181	0.379
0.81	0.22	0.395
0.85	0.264	0.42
0.88	0.34	0.467
0.91	0.36	0.501
0.95	0.4	0.529
0.98	0.42	0.552
1.01	0.45	0.59
1.05	0.48	0.623
1.08	0.497	0.657
1.11	0.528	0.691
1.15	0.561	0.71
1.18	0.593	0.735
1.21	0.607	0.752
1.25	0.63	0.8
1.28	0.66	0.819
1.31	0.69	0.842
1.35	0.715	0.876
1.38	0.742	0.912
1.41	0.766	0.964
1.45	0.781	0.996
1.48	0.806	1
1.51	0.829	1
1.55	0.854	1
1.58	0.866	1
1.61	0.893	1
1.65	0.905	1
1.68	0.931	1
1.71	0.97	1
1.75	0.997	1
1.78	1	1

Table B.6. Total Capacities of CO_2 over the TiO_2 Sorbent for Multiple Adsorption Cycles in the MVA Fluidized Bed in Figure 29

Cycle number	Adsorption capacity of CO_2 [mmol/g]
1	0.0841
2	0.0802

3	0.0791
4	0.0718
5	0.0689
6	0.0619
7	0.0612
8	0.0586

Table B.7. Breakthrough Curves of CO_2 over the TiO_2 Sorbent for 1st and 8th Adsorption Cycles in the MVA Fluidized Bed in Figure 30

Time [minutes]	C_{out}/C_{in}, 1st cylcle	C_{out}/C_{in}, 8th cycle
0.01	0	0
0.05	0	0
0.08	0	0
0.11	0	0
0.15	0	0
0.18	0	0
0.21	0	0
0.25	0	0
0.28	0	0
0.31	0	0.011
0.35	0	0.02
0.38	0	0.033
0.41	0	0.055
0.45	0	0.091
0.48	0	0.148
0.51	0	0.182
0.55	0.004	0.238
0.58	0.016	0.273
0.61	0.047	0.309
0.65	0.064	0.362
0.68	0.1	0.393
0.71	0.12	0.437
0.75	0.164	0.476

0.78	0.181	0.501
0.81	0.22	0.559
0.85	0.264	0.6
0.88	0.34	0.635
0.91	0.36	0.67
0.95	0.4	0.707
0.98	0.42	0.744
1.01	0.45	0.768
1.05	0.48	0.795
1.08	0.497	0.841
1.11	0.528	0.889
1.15	0.561	0.922
1.18	0.593	0.954
1.21	0.607	1
1.25	0.63	1
1.28	0.66	1
1.31	0.69	1
1.35	0.715	1
1.38	0.742	1
1.41	0.766	1
1.45	0.781	1
1.48	0.806	1
1.51	0.829	1
1.55	0.854	1
1.58	0.866	1
1.61	0.893	1
1.65	0.905	1
1.68	0.931	1
1.71	0.97	1
1.75	0.997	1
1.78	1	1

Software and UDF (User Defined Function) corresponding to Chapter 3

MFiX-19.2.0 and ParaView5.7.0 have been used for the simulation results.

User Defined Function for vibrational application to the TFM simulation.

```
SUBROUTINE USR1
    USE USR
    USE run
    USE constant
    IMPLICIT NONE
  REAL, PARAMETER :: A= 0.0002
  REAL, PARAMETER :: W= 314
  integer, parameter :: DOUBLE=kind(1.0d0)
  REAL(DOUBLE) :: SUMA
!  Include files defining statement functions here
  CALL_USR = .TRUE.
  A = 0.002   ! Vibration amplitude
  W = 314      ! Vibration angular frequency
  SUMA = 0   ! Initial condition
  SUMA = -A*W*W*SIN(W*TIME)
  GRAVITY_Y = GRAVITY_Y + SUMA    ! Y-direction Gravity
  RETURN
  END SUBROUTINE USR1
```

APPENDIX C

DATA FOR THE FIGURES IN CHAPTER 4

Carbon intensity by coal:

$$\frac{95.35 kgCO_2}{10^6 Btu} \times \frac{1\ Btu}{0.00029\ kWh} = 0.328\ \frac{kgCO_2}{kWh}$$

Energy used by MVA system (for 0.028 hours):

$$0.22kW \times 0.028\ hours = 0.0048\ kWh$$

Emitted Carbon Dioxide by using MVA system for :

$$0.328\ \frac{kgCO_2}{kWh} \times 0.0048\ kWh = 0.00157\ kgCO_2$$

Carbon Dioxide captured by MVA system (at first cycle):

$$0.083\ \frac{mmol\ CO_2}{g} \times 50\ g = 4.15\ mmol\ CO_2$$

$$4.15\ mmol\ CO_2 \times \frac{44.01 g}{1\ mol\ of\ CO_2} \times \frac{1\ kg}{1000\ g} \times \frac{1\ mol}{1000\ mmol} = 0.000116\ kgCO_2$$